Spin-orbit or Aharonov-Casher edge states in semiconductor systems

Lingling Xu

Dissertation submitted to the faculty of the Virginia Polytechnic Institute and State University in partial fulfillment of the requirements for the degree

of

Doctor of Philosophy

In

Physics

Jean J. Heremans, Chair
Victoria Soghomonian
Jonathan Link
Chenggang Tao

June 23, 2015
Blacksburg, VA

Keywords:

Aharonov-Casher effect, edge state, interference, magnetoresistance, antilocalization, InGaAs, spin-orbit strength

Spin-orbit or Aharonov-Casher edge states in semiconductor systems

Lingling Xu

Abstract

We present studies of edge states induced by the Aharonov-Casher vector potential or Rashba-type spin-orbit interaction using quantum transport in InGaAs/InAlAs herterostructures. The Aharonov-Casher effect is electromagnetically dual to the Aharonov-Bohm effect and is predicted to lead to edge states in a parabolic confinement at two-dimensional sample edges. As a narrow gap material, InGaAs has a low effective mass, high mobility, and strong spin-orbit interaction, which indicate that it can be used as a good material to detect the Aharonov-Casher effect or SOI interaction. Using InGaAs, we measured the magnetoresistance in a quantum antidot in narrow short channels in a tilted magnetic field. The fine structure (mT spacing) observed in the magnetoresistance indicate a probable energy spacing between AC edge states. We also fabricated side-gate channel structures in InGaAs/InAlAs quantum wells and investigated the values of the Rashba spin-orbit coupling constant α using the weak antilocalization analysis as a function of the side-gate voltage. We take the effect of the finite width into account and find the corrected values. With the simulation of electric fields in the wide channel and narrow channel, we found that the electric field components can be changed using side-gate voltages. While our results do not indicate which electric field component is responsible, the data indicate that the deduced α_{2D} values in a narrow channel are tunable by the side-gate voltage.

Dedication

To my loved family.

Acknowledgements

I would like to take this opportunity to express my heartfelt thanks to my advisor, Prof. Jean Joseph Heremans. He is such a knowledgeable scientist and a great mentor. I really appreciate his continuous support and guidance for all these years.

I would like to thank Prof. Victoria Soghomonian for giving me generous help and advice whenever I need it. I would also thank the rest of my committee, Prof. Jonathan Link and Prof. Chenggang Tao to be my committee members for giving me valuable comments and suggestions. I also want to thank all members in our lab: Dr. Ray Kallaher, Dr. Robert Lillianfeld, Dr. Yong-Jae Kim, Dr. Yao Zhang, Dr. Martin Rudolph, Dr. Qifan Yuan, Dr. Shaola Ren, and Yuantao Xie for great help and useful discussion.

Lastly, I must thank my husband and our parents for the invaluable support. And I have to thank my son Eason and my daughter Mia for the joy and sweet moment they have brought.

Table of Contents

List of Figures

Chapter 1. Introduction

1.1 Overview

In recent years, the Aharonov-Casher (AC) effect, an electromagnetic dual to the Aharonov-Bohm (AB) effect, has aroused a lot of interest both theoretically and experimentally [1-3], since it is not only crucial in fundamental scientific understanding of physics phenomena, but also has possible applications in the field of spintronics. The initial development of spintronics is based on the discovery of giant magnetoresistance (GMR) in ferromagnetic metal multilayers [4-6]. Magnetoresistance (MR) describes the effect that the electrical resistance of a material or device changes in response to the applied magnetic field B. In a GMR device, the electrical resistance is small when the magnetic moments of the ferromagnetic layers are parallel. The high electrical resistance of the antiparallel magnetic moments of ferromagnetic layers arises from the strong spin-dependent scattering of the carriers [7]. The orientation of the magnetic moments is controlled by an external magnetic field. Semiconductor spintronics combine semiconductor microelectronics with spin-dependent effects [8]. Its main advantage over ferromagnetic metal-based spintronics is its integrability with the extensive semiconductor fabrication [9]. Among the first semiconductor spin devices to be proposed was the Datta-Das spin field effect transistor (SFET) [10], which consists of ferromagnetic electrodes and a semiconductor two-dimensional electron system (2DES) channel with a gate electrode, as shown in Fig. 1.1 [11]. The source injects electrons with spin polarization parallel to the source polarization. The spin polarization is modulated by an electrostatic gate voltage through the spin-obit interaction (SOI) in the channel. When the electrons arrive at the drain, if the 2DES contains a substantial population of electrons with spin polarization aligned to the ferromagnetic drain electrode, a substantial current can flow into the drain electrode. Otherwise, the current is reduced. Thus, the ability to control and manipulate the electron spin requires efforts to investigate the mechanism of the spin splitting as well as the efficient control of the spin precession. In the thesis, we focus on the phenomena induced by AC vector potential or Rashba-type spin-orbit interaction (RSOI) to further understanding in the field of spintronics. We also propose a

side-gated channel to study if a side gate voltage can be used to control the Rashba spin-obit coupling constant in InGaAs/InAlAs heterostructure and how to utilize this method.

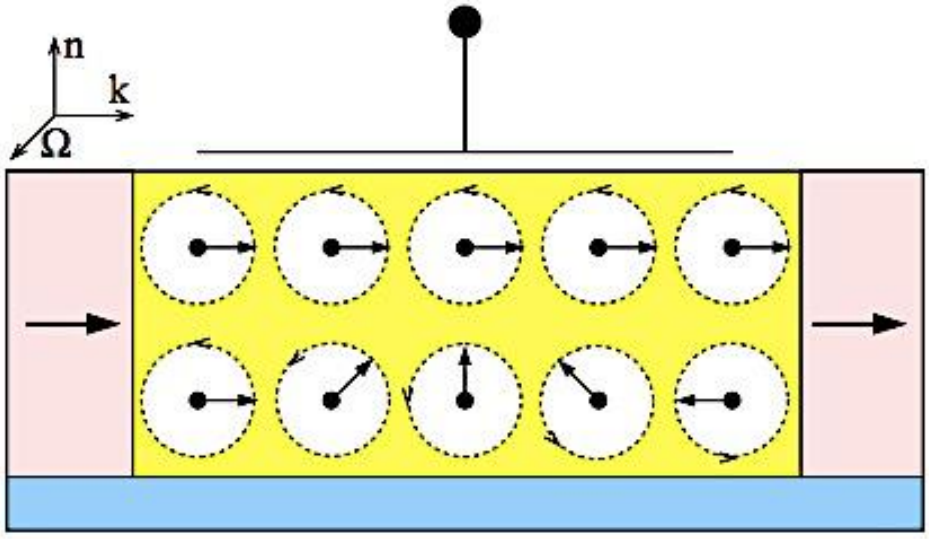

Figure 1.1 Scheme of the Datta-Das spin field-effect transistor (SFET) [10].

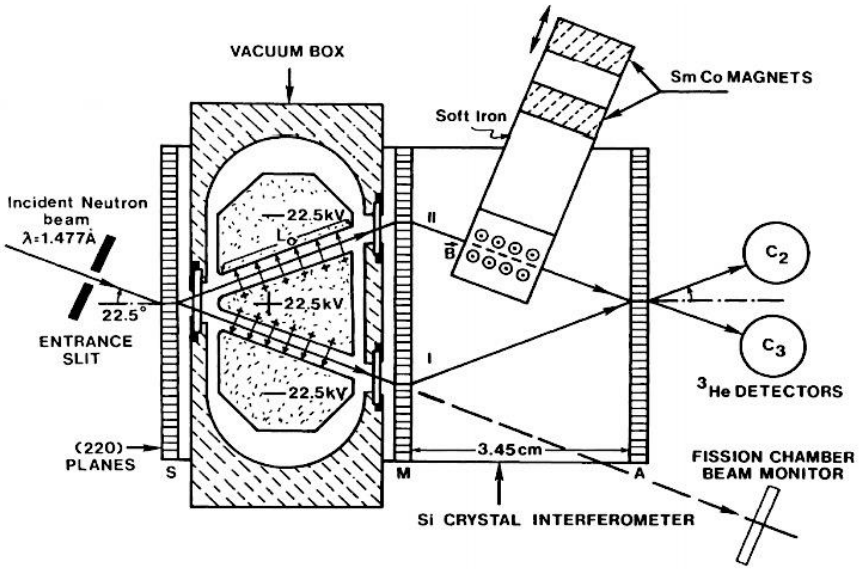

Figure 1.2 Experimental setup for an early detection of the AC effect [13].

The AC effect, proposed by Aharonov and Casher in 1984 [12], describes that a magnetic moment encircling a line charge acquires a quantum phase. The relative quantum shift was first observed in a neutron beam loop by Cimmino et al. [13]. In the experiment, the neutrons were sent to through a Mach-Zehnder interferometer consisting of three Bragg crystals (see Fig. 1.2). In our case, we surmise that the AC effective vector potential in a 2DES leads to helical edge states in a narrow channel geometry, forming travelling states at the sample edge in analogy to the integer quantum Hall effect (IQHE). The IQHE can be understood in terms of an edge channel picture [14, 15], in which each edge supports edge states traveling in only one direction. Unlike the IQHE, the propagation direction of the AC helical edge states also depends on the spin polarity. The helical edge states share similarities with those characterizing the quantum spin Hall effect (QSHE) [16]. Those spin-polarized channels are not fully understood and they are the subjects of active research both theoretically and experimentally [16-20].

Quantum interference of electrons including AC interference at low temperature leads to the phenomena of weak antilocalization (WAL) [21-23] and weak-localization (WL) [22, 23]. In a recent paper, the crossover transition from weak localization to weak antilocalization was observed in a narrow-gap InGaAs heterostructure by controlling the applied gate voltage [24]. The WAL analysis was used to deduce the zero-field spin splitting Δ_0. The dominant mechanism for the change in the SOI parameter was attributed to the Rashba term. In fact, the WAL analysis was utilized for studying Δ_0 by several other groups [25-28]. In our thesis, we use side-gated channel structures to control the SOI parameter by a gate voltage based on this method.

1.1 Classical magnetotransport

In a magnetic field, the movement of the electrons does not follow the direction of the electric field as the orbital motion of the electrons is curved by the magnetic field. In the Drude model in two dimensions, the relationship between the electric field $\boldsymbol{\varepsilon}$ and the current density $\boldsymbol{J}$ is defined as $\boldsymbol{J} = \hat{\sigma}\boldsymbol{\varepsilon}$ or equivalently $\boldsymbol{\varepsilon} = \hat{\rho}\boldsymbol{J}$, where $\hat{\sigma}$ is the (2×2) conductivity tensor and $\hat{\rho}$ is the resistivity tensor. For a single carrier system, the electron motion is described in the following equation:

$$m^*\left(\frac{d}{dt}+\frac{1}{\tau_m}\right)\boldsymbol{v}_d = -e(\boldsymbol{\varepsilon}+\boldsymbol{v}_d \times B) \tag{1.1}$$

where τ_m is the momentum relaxation time, m^* is the effective mass and $\boldsymbol{v}_d = \boldsymbol{J}/en$ is the drift velocity. In the stationary case, i.e. $d\boldsymbol{v}_d/dt = 0$, the resistivity tensor $\hat{\rho}$ can be expressed as follows:

$$\widehat{\boldsymbol{\rho}} = \frac{1}{ne\mu}\begin{pmatrix} 1 & -\mu B \\ \mu B & 1 \end{pmatrix} \tag{1.2}$$

where n, μ, e and B are carrier density, carrier mobility, electron charge, and magnetic field respectively. The resistivity at $B = 0$ is defined as $\rho = \frac{1}{ne\mu}$. The mobility of the sample is defined as $\mu = e\tau_m/m^*$. Classically the longitudinal resistance (diagonal terms) does not depend on B (no magnetoresistance) and the transverse magnetoresistance (Hall signal) is linear in B.

1.2 Quantum magnetotransport

The classical Drude model is only valid for a low magnetic field, when electrons are scattered before completing a cyclotron orbit, and if quantum corrections to the conductance do not enter the picture. At low temperature, a quantum mechanical approach has to be taken into account for high mobility samples.

1.2.1 Integer Quantum Hall effect

The Hamiltonian for a charged particle in an electromagnetic field can be written as

$$H_{AB} = \frac{1}{2m}(\boldsymbol{p} - q\boldsymbol{A})^2 + qV \tag{1.3}$$

where $\boldsymbol{A}$ is the vector potential and V is the confining potential in the 2DES. For the case $V = 0$, and if $\boldsymbol{B}$ is normal to the 2DES which we assume to lie in the x-y plane (so $\boldsymbol{B}$ // z), $\boldsymbol{A}$ is reasonably assumed to be ($-By$, 0, 0), the eigenenergies $E_n$and eigenwavefunctions for the Schrödinger equation are:

$$E_n = \hbar\omega_c \left(n + \frac{1}{2}\right), n = 0, 1, 2,\ldots \quad (1.4)$$

$$\psi_n(y) \propto e^{ik_x x} e^{-\frac{q^2}{2l_B^2}} H_n\left(\frac{q}{l_B}\right), q = y - k_x l_B^2 \quad (1.5)$$

where $\hbar$ is the Planck constant, m is the electron mass, the cyclotron frequency $\omega_c = eB/m$, the magnetic length $l_B = \sqrt{\hbar/eB}$, k_x is the wavevector and H_n is the Hermite polynomials. The discrete energy levels called "Landau levels" (LLs) are separated by the energy $\hbar\omega_c$ as shown in Fig. 1.3a. However in the channel geometry the finite width should be considered. In this case, the LL energy is lifted and intersects the Fermi level at the sample boundaries, where the edge states are formed. Current carried by the edge states flows at the different direction at the two sample edges without backscattering [14]. The classical behavior of electrons near the sample edge is shown in Fig. 1.3b to demonstrate the differences and similarities with the quantum case. Classically, electrons in the bulk of the sample move in a circular trajectory, known as a cyclotron orbit with no contribution to the current. In the quantum picture, the number of edge states in the sample corresponds to the number of the LLs intersecting the Fermi energy. Based on the formalism developed by Laudauer and Büttiker [29], the longitudinal resistivity ρ_{xx} distinguishes and the transverse resistivity forms plateaus with values $\rho_{xy} = h/ie^2$ (i is the number of edge states) when the Landau levels are completely occupied.

(a) (b)

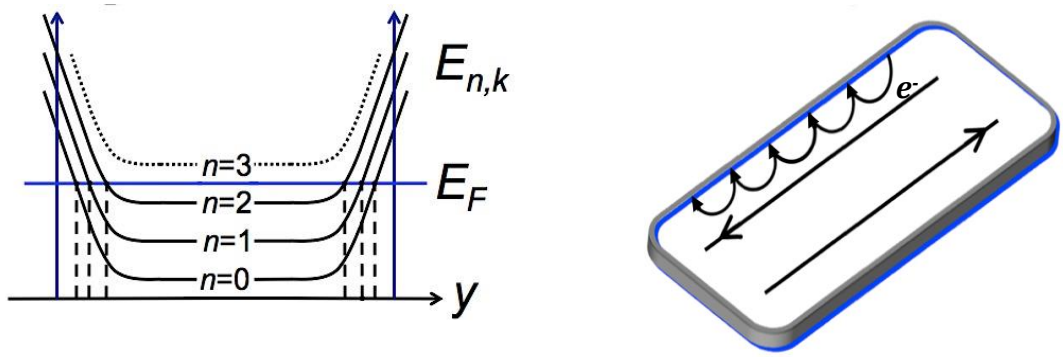

Figure 1.3 (a) The energy diagram of the Landau levels; (b) Schematic depiction of the classical orbits along the sample.

1.2.2 Aharonov-Bohm effect

Besides the discrete LLs, another quantum mechanical effect is the Aharonov-Bohm (AB) effect induced by the vector potential $\boldsymbol{A}$. It was proposed by Aharonov and Bohm [30] and occurs when electrons circle regions with a magnetic flux. The quantum phase associated with the effect is referred to as the AB phase [30], introducing an additional phase to the wavefunction given by the closed line l integral of A

$$\phi_{AB} = \frac{e}{\hbar}\oint \boldsymbol{A}\cdot d\boldsymbol{l} \tag{1.6}$$

A solid-state experimental realization of the AB effect is to measure the conductance change of mesoscopic rings (fabricated from metals such as Au, or from semiconductor heterostructures) dependent on the strength of the applied B [31]. The interference principle is in analogy to the two-slit experiment. The schematic geometry is illustrated in Fig. 1.4a, where the incoming electron traversing the ring structure is split into two parts and interference at the exit point. We assume Ψ_1 and Ψ_2 the wavefunctions of the top path and the bottom path with phase ϕ_1 and ϕ_2 respectively. The outgoing wavefunction follows the relationship below:

$$|\Psi_{out}|^2 = |\Psi_1|^2 + |\Psi_2|^2 + 2\,\mathrm{Re}(\Psi_1^*\Psi_2)\cos(\phi_2-\phi_1) + 2\,\mathrm{Im}(\Psi_1^*\Psi_2)\sin(\phi_2-\phi_1) \tag{1.7}$$

This probability amplitude, and hence the interference pattern, have a single periodicity in B, corresponding to a quantum flux h/e penetrating the ring area as explained below.

Also if $\phi_1 = \phi_2$ (left/right symmetric interferometer) then the periodic function is a pure cosine. It was theoretically pointed out the electrons acquire an additional phase $\phi = \frac{e}{\hbar}\oint \boldsymbol{A} \cdot d\boldsymbol{l} = \frac{e}{\hbar}\int B \times dS = \Phi 2\pi e/h$ along the closed loop with area S if the magnetic flux penetrated the ring is Φ, which equals to the phase difference between ϕ_1 and ϕ_2. The magnetic flux describes the amount of magnetic field passing through the a surface, which can also be written as the line integral of the vector potential along the loop

$$\Phi = \int B \times dS = \oint \boldsymbol{A} \cdot d\boldsymbol{l} \tag{1.8}$$

Thus the interference pattern is periodic in B with periodicity determined by the enclosed ring area. The AB oscillations were first observed in Au rings at low temperature T = 0.01 K, as displayed in Fig. 1.4b [31]. For interference to occur the wavefunction has to be coherent over the length of the ring arms. Thus the radius R of the ring should not much exceed l_ϕ/π in order to observe the AB oscillations, where l_ϕ is the phase coherence length.

(a) (b)

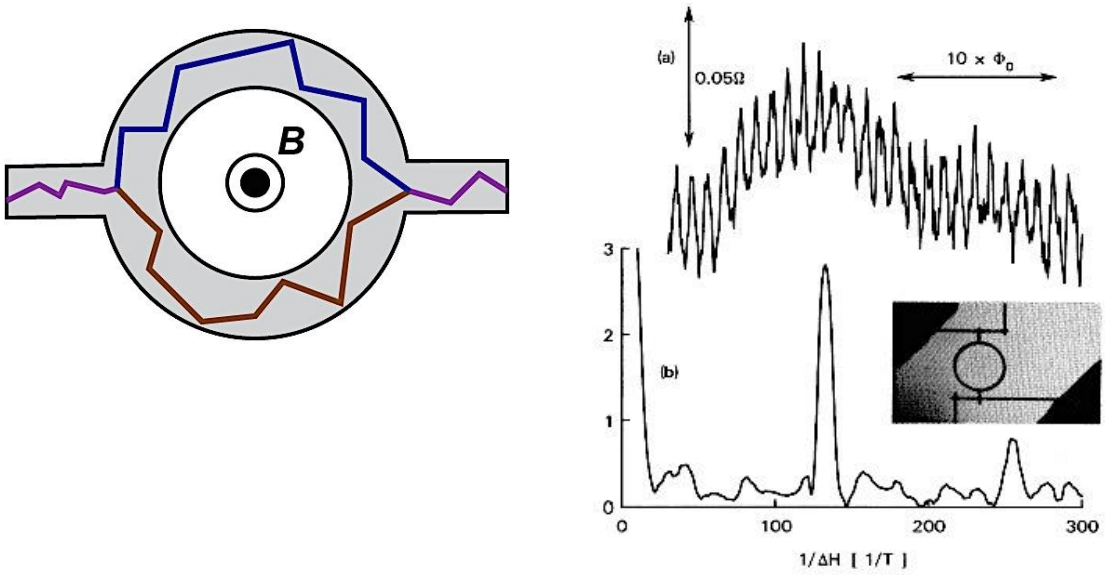

Figure 1.4 (a) Schematic representation of the Aharonov-Bohm effect in the ring structure; (b) Magnetoresistance oscillation as a function of applied magnetic field in Au ring [31].

Fourier analysis shows that there is another oscillation period of $h/2e$, which is so-called Altshuler-Aronov-Spivak (AAS) effect [31]. AAS oscillations are caused by interference of pairs of time-reversed paths at the entry point as depicted schematically in Fig. 1.5a. The clock-wise and counter-clockwise trajectories follow the exact same path but in opposite directions, which always results in constructive interference in the absence of magnetic flux. Contrary to the AB effect, the AAS effect can survive in a highly disordered device or in a series of many rings. However, the AAS effect is a low field phenomenon since the magnetic field breaks the time-reversal symmetry. The amplitude of AAS oscillation is rapidly reduced by B on the order of 10^{-3} T as seen in Fig. 1.5b [32].

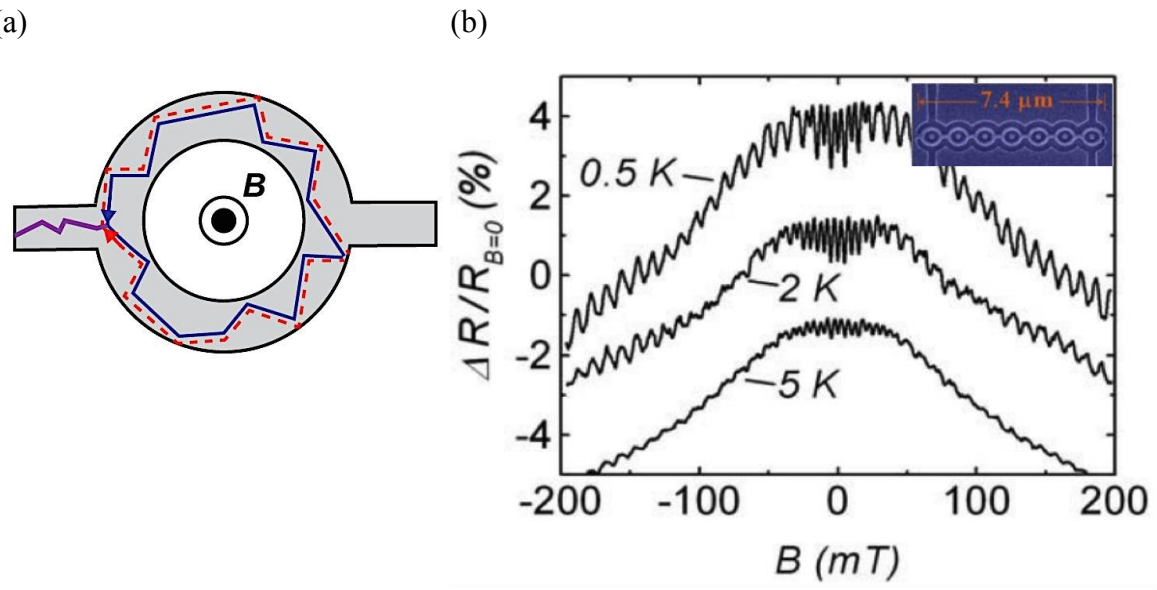

Figure 1.5 (a) Schematic representation of the Altshuler-Aronov-Spivak effect in the ring structure. (b) Resistance oscillations in an array of rings as depicted in the insert, with the oscillation amplitude falling off at higher B [32].

If the above rings are fabricated on material with SOI, the electron spin will precess around the magnetic field and spin interference will affect the interference at the entry point. For example, there is no interference if the spins of the red and blue line are opposite in Fig. 1.5a. The precession angle effectively modulates the AAS oscillation, which was expressed as a function of the RSOI parameter α,

$$\frac{\delta R_\alpha}{\delta R_{\alpha=0}} = cos\left\{2\pi\sqrt{1+\left(\frac{2m\alpha}{\hbar^2}r\right)^2}\right\} \tag{1.9}$$

where δR_α and $\delta R_{\alpha=0}$ are the AAS amplitude with or without SOI respectively, r is the radius of the ring and α is the SOI strength [33]. The oscillatory behavior is shown in Fig. 1.6 as a function of the gate voltage. The resistance was measured as a function of gate voltage as well as the magnetic field after digital filtering. In the ring array, the SOI strength α changes with the gate voltage. As the gate voltage changes, the AAS amplitude reduced to zero, which inverts the AAS oscillation. In the Fig. 1.6, we can clearly observe phase switching phenomena.

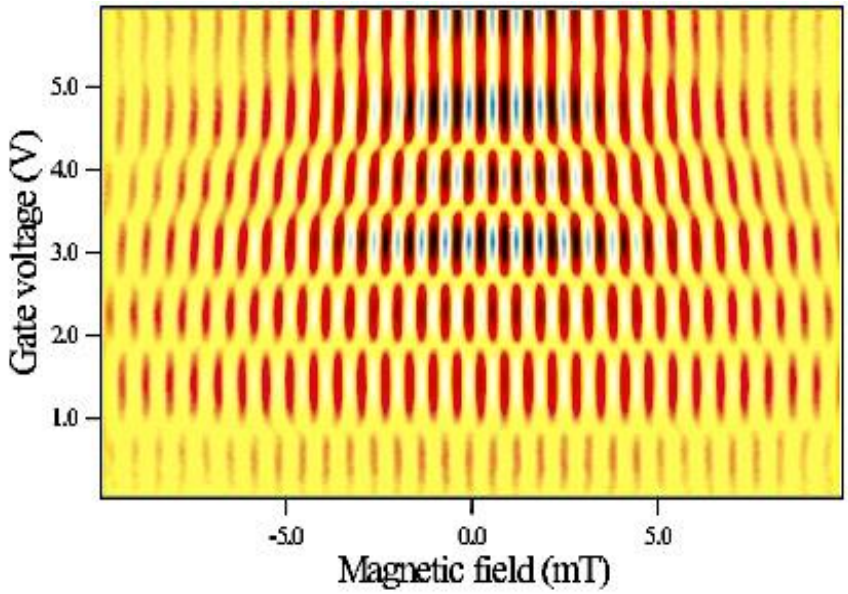

Figure 1.6 The resistance of a 5×5 ring array of radius 1.0 μm vs gate voltage and magnetic field after digital filtering which shows the AAS oscillations switch phase as the gate voltage increased in Ref. [33].

1.2.3 Spin-Orbit Interaction

Spin-Orbit Interaction (SOI) is a relativistic effect on a particle with spin moving in an electric field, linking the spin degree of freedom and the orbital degree of freedom. The spin-orbit Hamiltonian is given by:

$$H_{SO} = \frac{1}{4m_e^2c^2}\boldsymbol{p} \cdot [\boldsymbol{\sigma} \times \nabla V(r)] \tag{1.10}$$

where m_e is the free electron mass, c is the speed of light in vacuum, $\boldsymbol{p}$ is the momentum, σ are the Pauli matrices, and V(r) is the electrical potential experienced by electrons. The gradient of V(r), i. e. the electric field, leads to a spin precession around an axis perpendicular to the traveling direction and to the electric field itself. The electric field can be an actually applied field (as long as it does not integrate to zero over the wavefunction) or an effective field induced by spatial symmetry breaking. In the crystal structure, there are two origins for the effective electric field leading to SOI: the Dresselhaus and the Rashba interaction. The orientation of spin (or the precession axis) as a function of momentum is depicted in Fig. 1.7. The Rashba term arises from the structural-inversion asymmetry (SIA) [24, 34]. The electric field induced by the asymmetrical potential is in the 2DES, which breaks the space inversion symmetry, just as its dual, B breaks the time reversal symmetry. The spin precession caused by RSOI occurs around the k_x direction along k_y direction and vice versa, as shown in Fig. 1.7a. The Hamiltonian to describe this can be expressed:

$$H_R = \alpha(\sigma_x k_y - \sigma_y k_x) \tag{1.11}$$

The parameter α is linearly dependent on the expectation value $< \varepsilon >$ of the (real or effective) electric field at 2DES in the heterostructure. Besides the SIA, there are multiple mechanisms causing Rashba-type SOI, such as lattice-strain effect, band discontinuity and so on. In some experiments, it was demonstrated that the Rashba SOI could be modulated by applying external gate voltage in different materials [3, 24].

The Dresselhaus SOI appears in semiconductor crystals with broken bulk-inversion symmetry, which typically happens in zinc-blende crystal lattice structures [34]. The corresponding Hamiltonian can be written as the sum of a linear and a cubic term:

$$H_D^{(1)} = \beta(\sigma_x k_x - \sigma_y k_y) \tag{1.12}$$

$$H_D^{(3)} = \gamma(\sigma_y k_y k_x^2 - \sigma_x k_x k_y^2) \tag{1.13}$$

where the strength of linear BIA induced spin splitting $\beta = \gamma\langle k_z^2 \rangle$ depends on the width of the wavefunction along the confinement direction *z* direction. Fig. 1.7b and Fig. 1.7c show the spin (precession axis) orientation for the linear and cubic term respectively. In an InGaAs 2DEG, the Dresselhaus SOI is usually smaller than the Rashba SOI. Thus in the thesis, we only focused on H_R by neglecting $H_D^{(1)}$ and $H_D^{(3)}$ to fit the low-field magnetoconductance data.

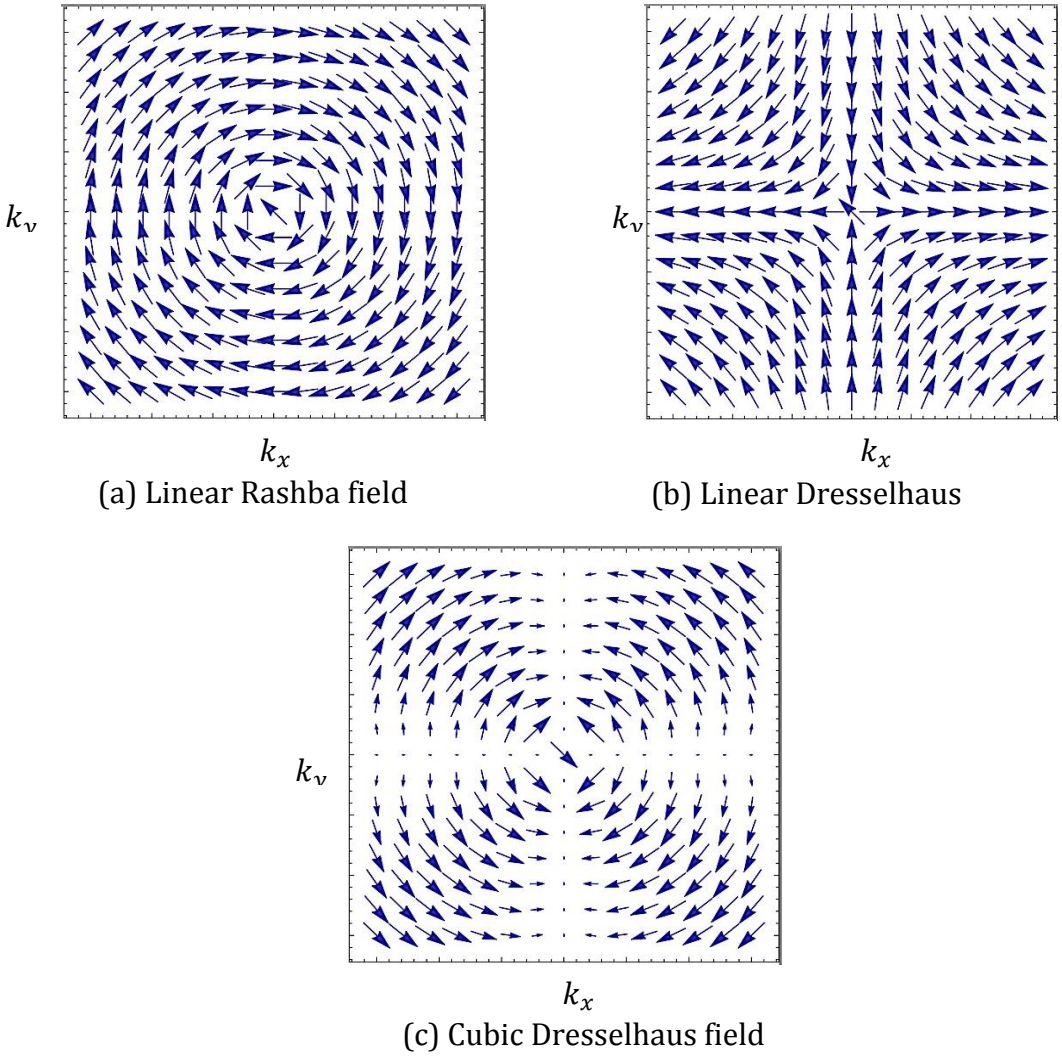

(a) Linear Rashba field (b) Linear Dresselhaus

(c) Cubic Dresselhaus field

Figure 1.7 Schematic sketches of the spin orientation (precession axis orientation) due to Rashba and Dresselhaus effects. Here k_x is chosen to be [010], k_y the [100] crystal direction and z is along [001].

1.2.4 Weak localization (WL) & Weak antilocalization (WAL)

In the Drude model, electrons were treated as classical particles moving in an idealized ballistic system but ignored are the quantum interference contributions to transport as shown in Fig. 1.8a. In the 1980s, the phase-coherent multiple scattering by impurities, defects and phonons was taken into account systematically. The interference between the time-reversed paths results in enhancing of the backscattering of the electron wave, known as weak-localization (WL). As illustrated in Fig. 1.8b, considering an electron propagating from A to B along a random path, the quantum mechanical superposition indicates that the probability of finding the electron at point B is given by [35]

$$P = |\psi_1 + \psi_2 + \cdots + \psi_n|^2 = P_1 + P_2 + \cdots + P_n + \sum_{i \neq j}^{n} (\psi_i \psi_j^* + \psi_i^* \psi_j) \qquad (1.14)$$

where ψ_i represent the individual path's partial wavefunctions, ψ_i^* is the complex conjugate of ψ_i and the square of ψ_i yields probability P_i. The sum of P_i is classical contribution to the Drude-Boltzman theory. The last term is the interference term, which is important for the WL correction. The large number of random scatterings averages out the interference term, leaving the classical probability for propagating trajectories. However, a special situation arises if we consider the time-reversed paths as depicted in Fig. 1.8c. The two partial waves propagating clockwisely and counter-clockwisely along the loop paths return to the starting point after identical scattering, which results in constructive interference. The backscattering probability is $P = |\psi_1 + \psi_2|^2 = 4|\psi_1|^2$ due to the equal probability amplitudes and the phases of the two time-reversed paths. Compared to the classical probability of $2|\psi_1|^2$, the increased backscattering manifests itself as a negative quantum correction to the conductivity, the WL correction. The observation of WL relies much on the phase coherence length l_ϕ. If the lengths of the time-reversed paths exceed l_ϕ, the interference cannot happen since the phase is no longer coherent. The application of a normal magnetic field $\boldsymbol{B}$ breaks the time reversal symmetry, suppress the WL, and thus leads to a negative magnetoresistance around zero *B* as depicted in Fig. 1.9a.

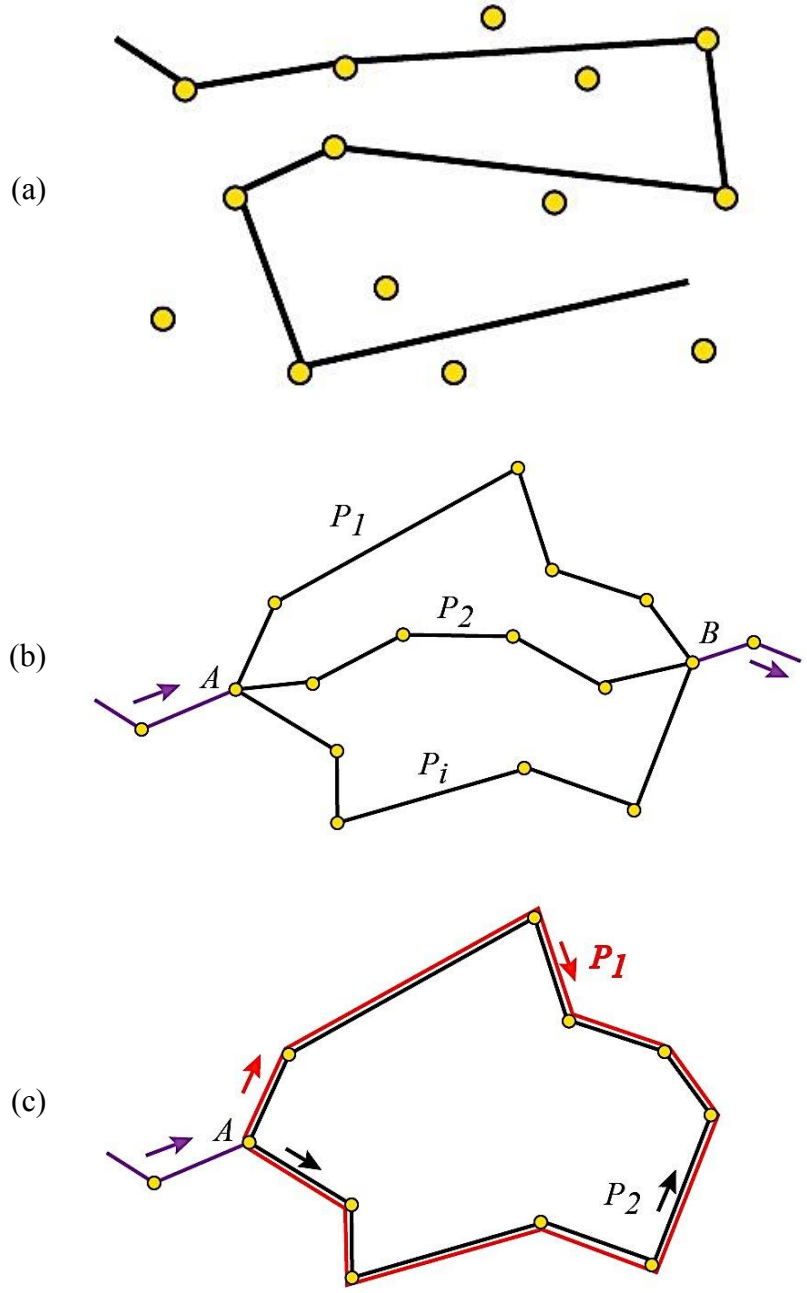

Figure 1.8 Schematic illustration of different electronic transport in solids. Yellow dots represent impurities. (a) Ballistic trajectory. (b) Multiple scattering paths from point A to point B in a disordered system. (c) Time-reversed paths shown by red and black lines.

In the WL effect, the spins of the particles are not taken into account. If a material has a strong SOI, the change in phase of spin states causes an additional phase shift π to the time-reversed loop paths, which leads to destructive interference. The probability of backscattering is thus reduced and the conductivity increased. The relative phase difference is 2π while ½ spin state has a rotational periodicity of 4π, which leads to destructive interference with suppressed backscattering probability $P = |\psi_1 - \psi_1|^2 = 0$. The decrease of the probability manifests itself as a positive correction to the conductivity, which is called weak antilocalization (WAL) effect, the opposite effect of WL [36, 37]. The SOI strength is measured by the spin orbit length l_{so}: a stronger SOI results in a shorter l_{so}. As the electron propagates along the path, the spin orientation is randomized over the length scale l_{so}. For the system where $l_\phi < l_{so}$, SOI is negligible and WL dominates (see Fig. 1.9a). In the opposite case of $l_\phi > l_{so}$ (strong SOI), electrons under SOI still maintain their phase coherence after being scattered for many times, which results in an antilocalization minimum at $B = 0$ (see Fig. 1.9c). In the intermediate case, $l_\phi \approx l_{so}$, where trajectories affected by SOC needs to be rather long but are still shorter than the coherence length, the destructive interference only occur at lowest *B* while the constructive interference dominants at higher *B*. The weak localization peak develops an antilocalization dip at small peak as depicted in Fig. 1.9b.

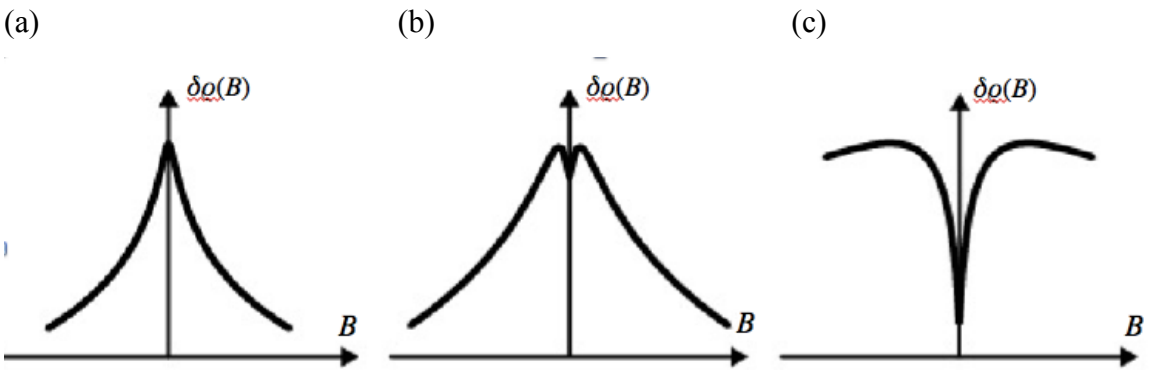

Figure 1.9 Magnetoresisatance under weak localization phenomena for different SOC regimes: (a) $l_\phi < l_{so}$; (b) $l_\phi \approx l_{so}$; (c) $l_\phi > l_{so}$.

1.2.5 Aharonov Casher effect

The Aharnov-Casher (AC) effect is analogous with the AB effect from several perspectives. The AB effect is a phenomenon in which a charged particle moves around a stationary solenoid. The AC effect couples the movement of the magnetic moment with the electric field. The corresponding AC vector potential is given by $\frac{1}{c^2}\boldsymbol{\mu} \times \boldsymbol{\varepsilon}$, with spin playing a role of isospin [38], where c is the speed of light, μ is the magnetic moment and ε is the electric field. Unlike the AB effect, the AC vector potential does not necessarily involve the gauge symmetry. Since it couples the spin with the orbit, it would break the time reversal symmetry and hence give antilocalization as the SOI. As a consequence of the fact that the electric field ε is locally measurable, the vector potential should be observable whereas the magnetic vector potential only has observable consequences over an effectively closed loop integral. And also the induced AC phases of open or closed path are physical [39]. The AC phase along the loop l is described as:

$$\phi_{AC} = \frac{1}{\hbar c^2}\oint \boldsymbol{\mu} \cdot \boldsymbol{\varepsilon} \times dl \tag{1.15}$$

Neglecting the electron-electron interactions, if there is magnetic field, the Hamiltonian can be written as [39]:

$$H_{AC} = \frac{1}{2m_o}(\boldsymbol{p} - e\boldsymbol{A})^2 + V + \frac{e\hbar}{2m_o}\boldsymbol{\sigma} \cdot \boldsymbol{B} - \frac{e\hbar\boldsymbol{\sigma}\cdot(\boldsymbol{p}-e\boldsymbol{A})\times\boldsymbol{\varepsilon}}{4m_o^2c^2\hbar} - \frac{e\hbar^2}{8m_o^2c^2}\nabla \cdot \boldsymbol{\varepsilon} + V \tag{1.16}$$

where the first and the second terms are the kinetic energy and the potential. The third term is the Zeeman term where $\boldsymbol{B}$ is the magnetic field and $\boldsymbol{\sigma}$ is the Pauli matrix vector. The fourth and the fifth term is the spin-orbit interaction and the Darwin terms where $\boldsymbol{\varepsilon}$ is the electric field and c is the speed of light. If the potential is static, i.e., $\boldsymbol{\nabla} \times \boldsymbol{\varepsilon} = \boldsymbol{0}$, the Hamiltonian can be expressed as [39, 40]:

$$H_{AC} = \frac{1}{2m_o}(\boldsymbol{p} - e\boldsymbol{A} - \frac{2m_o}{\hbar^2}\boldsymbol{s} \times \boldsymbol{\lambda})^2 + \frac{1}{2}\nabla \cdot \boldsymbol{\lambda} - \frac{2}{\hbar}\mu_B \boldsymbol{s} \cdot \boldsymbol{B} - \frac{m_o\boldsymbol{\lambda}^2}{2\hbar^2} + V \tag{1.17}$$

where $\boldsymbol{\lambda} = -\frac{e\hbar^2}{4m_o^2c^2}\boldsymbol{\varepsilon}$ and $s = h\sigma/2$for spin ½. The additional term of $\frac{2m_o}{\hbar^2}\boldsymbol{s}\times\boldsymbol{\lambda}$ in the square equals to $\frac{1}{\boldsymbol{c^2}}\boldsymbol{\mu}\times\boldsymbol{\varepsilon}$ corresponding to the AC term. To pull this term into the kinetic energy term, higher-order terms appear in the Eq. 1.17. The higher-order term $\frac{1}{2}\nabla\cdot\lambda$ is the Darwin term which corresponds to $-\frac{\mu\hbar}{2m_oc^2}\nabla\cdot\boldsymbol{\varepsilon}$ and another one $-\frac{m_o\lambda^2}{2\hbar^2}$ equals to $-\frac{\mu^2\varepsilon^2}{mc^4}$, where the magnetic moment $\mu = -\frac{e\hbar}{4m_o}$, which confirms that Eq. 1.17 is consistent with the result in Amanda's Anandan's paper [41]. For the Zeeman term $-\frac{2}{\hbar}\mu_B\boldsymbol{s}\cdot\boldsymbol{B}$, with $\boldsymbol{s} = \frac{\hbar}{2}\boldsymbol{\sigma}$, it can be rewritten as $-\mu_B\boldsymbol{\sigma}\cdot\boldsymbol{B} = -2\mu\boldsymbol{\sigma}\cdot\boldsymbol{B}$, as if $g = -2$ compared to the Anandan's paper. From the existence of the AC term in the kinetic energy, the gauge symmetry is broken. Assuming the magnetic field is zero, if the two higher-order terms are negligible, the Hamiltonian in the parabolic potential can be written as:

$$H_{AC} = \frac{1}{2m}\left(\boldsymbol{p} - \frac{1}{c^2}\,\boldsymbol{\mu}\times\boldsymbol{\varepsilon}\right)^2 + \frac{1}{2}\omega_p^2y^2 \tag{1.18}$$

In Chapter 3, the above equation will be analyzed in detail.

1.3 References

1. L. Xu, S. Ren, and J. J. Heremans, Integr. Ferroelectr. 131, 36–46 (2011).

2. H. Mathur and A. D. Stone, Phys. Rev. Lett. 68, 2964 (1992).

3. J. Nitta, T. Akazaki, H. Takayanagi, and T. Enoki, Phys. Rev. Lett. 78, 1335 (1997).

4. M. N. Baibich, J. M. Broto, A. Fert, F. Nguyen van Dau, F. Petroff, P. Eitenne, G. Creuzet, A. Friederich, and J. Chazelas, Phys. Rev. Lett. 61, 2472 (1988).

5. G. Binasch, P. Grunberg, F. Saurenbach, and W. Zinn, Phys. Rev. B 39, 4828 (1989).

6. B. Dieny, V. S. Speriosu, S. S. P. Parkin, B. A. Gurney, D. R. Wilhoit, and D. Mauri, Phys. Rev. B 43, 1297 (1991).

7. N. F. Mott, Proc. R. Soc. London, Ser. A 153, 699 (1936).

8. A. Fert, J. -M. George, H. Jaffr`es and R. Mattana, IEEE Trans. Elec. Dev. 54, 921 (2007).

9. M. B. A. Jalil, S. G. Tan, and T. Fujita, AAPPS bulletin, 18, 9 (2008).

10. S. Datta, B. Das, Appl. Phys. Lett. 56, 665 (1990).

11. I. Zutic, J. Fabian, and S. Das Sarma, Rev. Mod. Phys., 76, 323 (2004).

12. Y. Aharonov and A. Casher, Phys. Rev. Lett. 53, 319 (1984).

13. A.Cimmino, G.I. Opat, A.G. Klien, I-I. Kaiser, S.A. Werne M. Arif and R. Clothier, Phys. Rev. Lett. 63, 380 (1989).

14. B. I. Halperin, Phys. Rev. B 25, 2185 (1982).

15. A. H. MacDonald, and P. Streda, Phys. Rev. B 29, 1616 (1984).

16. C. L. Kane, and E. J. Mele, Phys. Rev. Lett. 95, 226801 (2005).

17. B. A. Bernevig, T. A. Hughes, and S. C. Zhang, Science 314, 1757 (2006).

18. M. Konig, S. Wiedemann, C. Brne, A. Roth, H. Buhmann, L. W. Molenkamp, X. L. Qi, and S. C.Zhang, Science 318, 766 (2007).

19. L. Fu, C. L. Kane, and E. J. Mele, Phys. Rev. Lett. 98, 106803 (2007).

20. J. E. Moore, and L. Balents, Phys. Rev. B 75, 121306(R) (2007).

21. S. Hikami, A. I. Larkin, and Y. Nagaoka,Prog. Theor. Phys, 63:707, (1980).

22. G. Bergmann. Phys. Rep., 107, 1 (1984).

23. S. McPhail, C. E. Yasin, A. R. Hamilton, M. Y. Simmons, E. H. Linfield, M. Pepper, and D. A. Ritchie, Phys. Rev. B, 70, 245311 (2004)

24. T. Akazaki, N. Takayuki, M. Kohda, and J. Nitta, Physica Status Solidi C 3, 4243 (2006).

25. G. L. Chen, J. Han, T. T. Huang, S. Datta, and D. B. Janes, Phys. Rev. B 47, 4084 (1993).

26. P. D. Dresselhaus, C. M. A. Papavassiliou, R. G. Wheeler, and R. N. Sacks, Phys. Rev. Lett. 68, 106 (1992).

27. T. Koga, J. Nitta, T. Akazaki, and H. Takayanagi, Phys. Rev. Lett. 89, 046801 (2002).

28. J. B. Miller, D. M. Zumbuhl, C. M. Marcus, Y. B. Lyanda-Geller, D. Goldhaber-Gordon, K. Campman, and A. C. Gossard, Phys. Rev. Lett. 90, 076807 (2003).

29. S. Datta, “Electronic Transport in Mesoscopic Systems” (Cambridge university press, 1995).

30. Y. Aharonov and D. Bohm, Phys. Rev. 115, 485 (1959).

31. R. A. Webb, S. Washburn, C. P. Umbach, and R. B. Laibowitz, Phys. Rev. Lett. 54, 2696 (1985).

32. R. B. Lillianfeld, R. L. Kallaher, J. J. Heremans, Hong Chen, N. Goel, S. J. Chung, M. B. Santos, W. Van Roy, and G. Borghs, Physics Procedia 3, 1231 (2010).

33. T. Bergsten, T. Kobayashi, Y. Sekine, and J. Nitta, Phys. Rev. Lett. 97, 196803 (2006).

34. M. Wu, J. Jiang, and M. Weng, Physics Reports, 493, 61 (2010).

35. C. W. J. Beenakker and H. van Houten, Solid State Phys., 44,1(1991).

36. S. Hikami,A. I. Larkin, and Y. Nagaoka, Physics 63, 707 (1980).

37. Y. B. Lyanda-Geller, and G. Pikus, JETP Lett 60 (1994).

38. A. S. Goldhaber, Phys. Rev. Lett. 62, 482 (1989).

39. E. Medina, A. Lopez and B. Berche, EPL, 83, 47005 (2008).

40. P. Q. Jin, Y. Q. Li, and F. C. Zhang, J. Phys. A: Math. Gen., 39, 7115 (2006).

41. J. Anandan, Phys. Lett. A, 138, 347 (1989).

Chapter 2. Fabrication and Measurement Techniques

In this chapter, we mainly discuss the fabrication processes for realizing specialized mesoscopic structures, which includes photolithography and electron-beam lithography. The techniques used to measure the magnetotransport properties at low temperature are also explained.

2.1 Sample fabrication

The material used in the thesis is a $In_{0.64}Ga_{0.36}As/In_{0.45}Al_{0.55}As$ heterostructure grown by molecular-beam epitaxy (MBE) system on semi-insulating InP (001) substrate. As can be seen in Fig. 2.1a, the 10 nm wide $In_{0.64}Ga_{0.36}As$ quantum well (QW) is located 50 nm below the surface. Fig. 2.1b shows the conduction band profile of a QW with a δ-doping layer [1]. Electrons are provided to the well by Si δ-doped layers separated by 18 nm $In_{0.45}Al_{0.55}As$ layer above the well. The electrons in the QW form the 2DES. The Hall–effect measurements indicate the 2DES electron density $N_S \approx 1.0 \times 10^{16}$ m^{-2} and the mobility $\mu \approx 5.9$ m^2/Vs at T = 0.4 K.

After the description of the information of the material, the general fabrication steps that are performed to transfer the specific pattern to the film are presented. The complete fabrication process includes three steps: the Hall bar patterning, the small structure definition, and the realization of the ohmic contacts.

The first step of the device fabrication is to cut a 3×3 mm^2 InGaAs sample from the InGaAs wafer. The sample is cleaved by making a line scratch on the backside of the wafer with a carbide pin, then pressing gently on the topside of the wafer to cleave alone the line. The surface of the wafer always keeps in touch with the lens paper in order to avoid scratches. To get rid of organic contamination from the sample's surface, a sequence of chemistries is used to clean the sample. The standard cleaning consists of: 3 minutes in TCE (trichloroethylene), 3 minutes in ACE (acetone) and 3 minutes in IPA (isopropyl alcohol). After the cleaning sequence, the IPA is squirted on the sample and the sample is blown dry with nitrogen gas. The cleaned sample is glued to a corner of an

18 × 18 mm^2 glass slide for easily handling. The glass slide with the sample is baked at 95 ˚C in an oven for 15-30 minutes.

(a) (b)

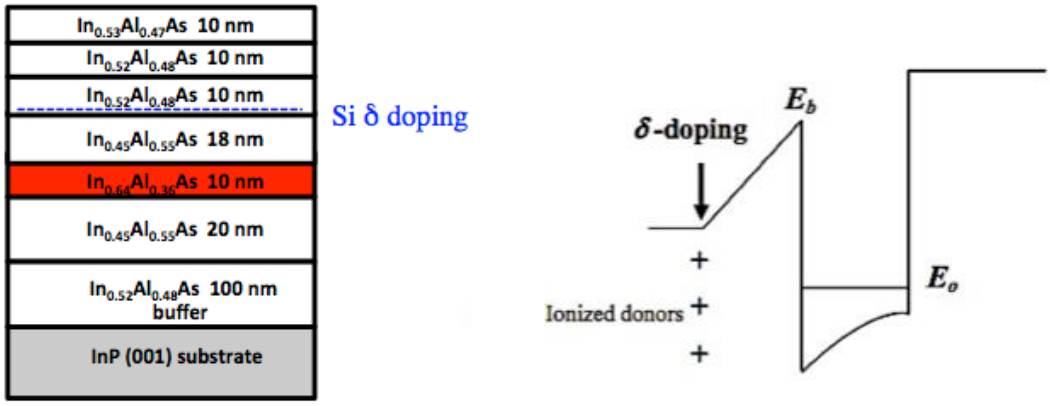

Figure 2.1 (a) The layout of the $In_{0.64}Ga_{0.36}As/In_{0.45}Al_{0.55}As$ heterostructure used in the thesis to fabricate devices. (b) The conduction band of QW with a δ-doping layer [1].

The sample is now ready for patterning the Hall bar that defines the current and voltage probes. Photolithography is known as a common method to define the Hall bar structure on the sample. It is the process to transfer a pattern from a mask to the substrate. The processing steps of photolithography and the etching steps are illustrated in Fig. 2.2. In the dark room, the glass slide with the sample is mounted onto a spin-coating machine (Specialty Coating Systems model P-6000). The top surface of the sample is covered with a few drops of an ultraviolet (UV) light sensitive material called photoresist (AZ5206E) and spun with high speed (4000 rpm) for 40 s to produce a thin, uniform coating about 600 nm thick. After spinning, a 30 minutes bake at 95 ˚C is performed to cure the photoresist and drive solvent out of the resist. The photomask, a glass plate with patterned iron oxide material on one side, is aligned to the sample using a Karl Suss (model MJB3) photolithography machine and the photoresist is exposed to a UV light with a mercury lamp (Hg light source, λ = 365 nm). The UV exposure time is 23 s. The patterned part of the mask is completely opaque to the light and the rest part is transparent. The exposed area becomes more soluble in the developer (AZ351) since it

undergoes chemical reaction. The sample is developed by immersing it in this particular developer for 15 s to dissolves the exposed portion, followed by rinsing it in de-ionized water for at least 1 minute. Then the desired pattern is left on the top of the sample. The sample is etched in a solution of H_3PO_4 : H_2O_2 : H_2O with ratio 1 : 1 : 38 for 120 s to remove the 2DES outside the desired region. After etching is completed, the photoresist is stripped off by 3-hour ACE cleaning process: soaking the sample in ACE for 1 hour, boiling the sample in ACE (75 ˚C) for 1 hour and then immersing it in fresh ACE at room temperature for another 1 hour.

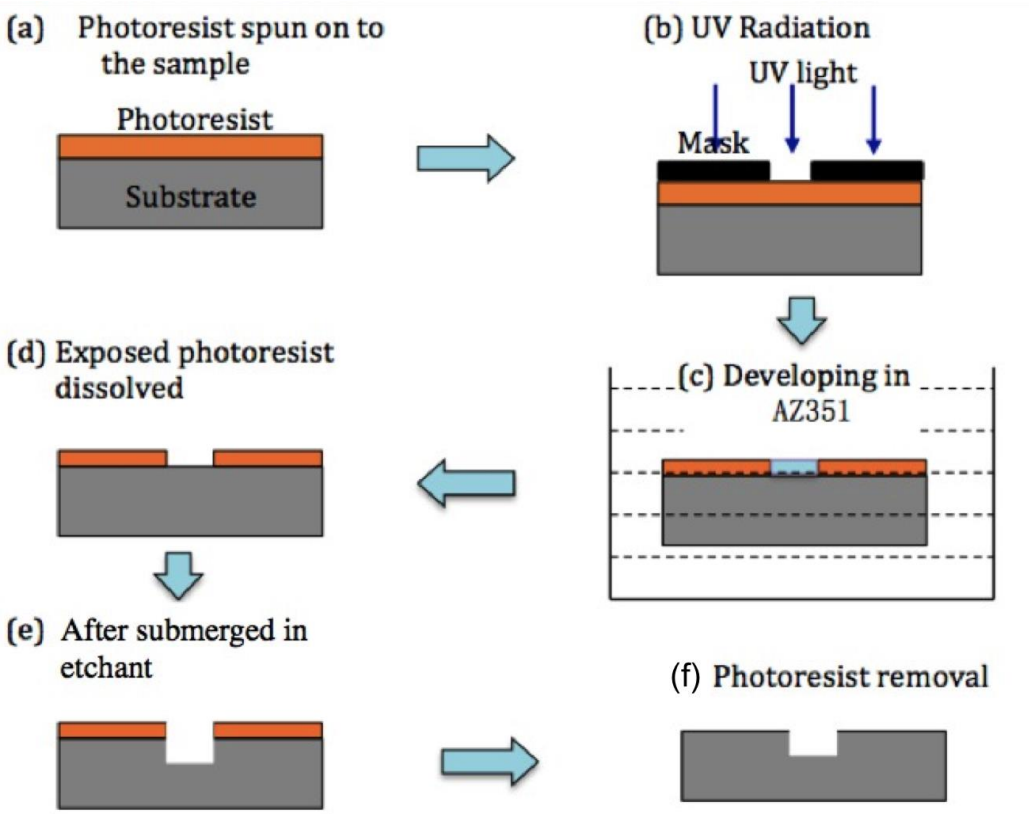

Figure 2.2 The schematic for fabrication of Hall bar structure. (a)~(d) Photolithography process and (d)~(f) the etching process.

The second step is to define smaller structure onto the Hall Bar mesa by electron-beam lithography. Before this step, small dot of InSn alloy is placed on the contacting pads of the Hall bar mesa to work as ohmiccontact using a micro-soldering iron (Weller WD1M with a Weller RT1 Needle Tip). InSn is approximately 50% Indium and 50% tin with melting point 117 ˚C. At the alloying temperatures, it can easily diffuse from the surface

to the conducting QW layer. And it is also very stable and conductive at low temperature (0.4 K). The soldering temperature is set to around 200 ˚C. When all the contacts are added, the sample is annealed in a homemade annealing station in forming gas at 210 ˚C for 5 minutes. The sample is ready for electron-beam lithography, which is similar to photolithography. The process is to direct a focused electron beam from a scanning electron microscope (SEM) across a resist layer and create geometric patterns. The resist used in the thesis is 950 K polymethylmethacralate (PMMA), which is dissolved in chlorobenzene with 3% concentration. Before depositing PMMA, the sample is glued on a glass slide covered with conducting metal such as gold to drain electrons, using colloidal graphite. The sample is dried at room temperature for 15 minutes, and then baked in a 170 ˚C for 30 minutes. The PMMA is spun onto the sample at 7800 rpm for 40 s, followed by baking in the 170 ˚C oven for 6 hours. The sample is inserted into the SEM chamber and the chamber is evacuated, bringing the system pressure down to 5 × 10-5 Torr. The electron beam is controlled by NPGS (Nano-Pattern Generating System) software. The process includes two parts, writing pattern and running the pattern. Writing the pattern is done in a CAD (computer-aided design) program that is linked to NPGS. Running the pattern includes specifying parameters such as the area or line dosage, the center-to-center distance, the magnification and so on. Depending on the information, NPGS calculates the exposure time and the deflection voltages supplied to the SEM in order to place each point correctly. The electron scattering in the PMMA and the substrate often leads to exposure regions surrounding the area where the electron beam is incident, which is referred to as the proximity effect. Therefore when regions are close to one another, lower dosage is needed. For example, a single dot (~ 40 nm in diameter) is written with a dose of 220 $\mu C/cm^2$. However, for a line (~ 40 nm), a dose of only 140 $\mu C/cm^2$ is necessary. Once the PMMA is exposed, the sample is developed by immersing in methyl isobutyl ketone (MIBK) diluted 3 times with IPA, for 70 s. Immediately after, the sample is rinsed in IPA for ~ 30 s and blown dry with nitrogen. The pattern is transferred to the sample by inductively coupled plasma reactive-ion etching (ICP-RIE). ICP-RIE is a type of dry etching, which uses chemical reactive plasma to remove material deposited on the sample. The system consists of a cylindrical plasma chamber where the wafer platter is put at the bottom portion of the chamber. The plasma is

generated with an RF (radio frequency) electromagnetic field, causing high-energy ions to bombard the wafer surface and react with it. Etch conditions vary for different materials, which depend strongly on pressure, gas flow, RF power and so on. In the experiment, the etching process is conducted with InGaAs recipe. For the typical structure, the process time is set to 40 s. After etching, the PMMA is removed by the 3-hour ACE cleaning process. The sample is ready to package into a standard 14 dual-in-line package (DIP) form. All contacting pads need to be electrically connected to the pins of an empty 14 pin DIP header by soldering Au wires with In (Indium). The soldering temperature is set to be 220 ˚C-240 ˚C. The sample is attached to the DIP header by Apiezon N low temperature grease, which makes the sample stick on the header even at low temperature (0.4 K).

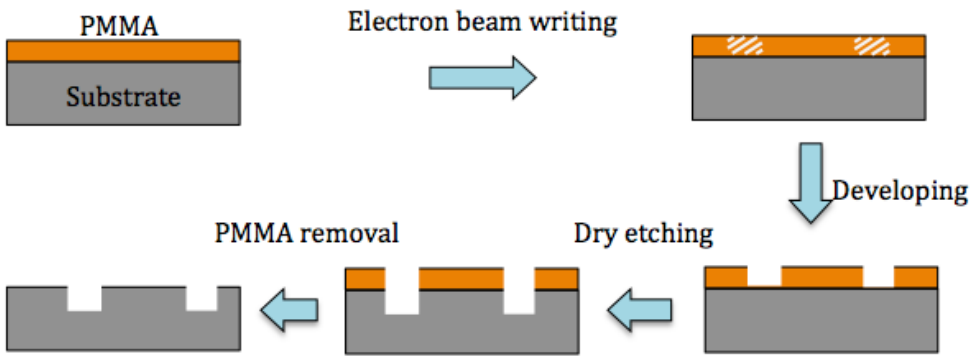

Figure 2.3 Schematic overview of the procedure to fabricate the small structure.

2.2 Measurement Setup

Transport measurements are carried out with a low temperature system (Fig. 2.4), using a combination of ^{4}He and ^{3}He cryogenic techniques. The ^{4}He system is capable of 4.2 K or 1.5 K in a steady state. Some magnetoresistance measurements are carried out above 1.5 K in a ^{4}He cryostat with a superconducting magnet that has maximum magnetic field 9 T. ^{3}He is not necessary in the innermost chamber. The ^{3}He system can be cooled to as low as 1.5 K in a steady state. Some magnetoresistance measurements are carried out above 1.5 K in a ^{4}He cryostat with a superconducting magnet that has maximum magnetic field

9 T. ^{3}He is not necessary in the innermost chamber. The ^{3}He system can be cooled to as low as Fig. 2.5. The entire cooling assembly was encased in a can with several chambers filled with liquid He. Lower temperature is achieved by pumping over the liquid He. Calibrated thermometers and resistive heaters are inserted into the cryostats to control the temperature.

Figure 2.4 Picture of measuring setup. Equipment consist of a LakeShore 370 AC resistance bridge, Princeton Applied Research P124A analog lock-in amplifier, SR 830 digital lock-in amplifier, EG&G 7265 digital lock-in amplifier, Keithley 2400 source meter, Keithley 2000 multimeter, Yokogawa GS200 voltage sources, Cryomagnetics CS-4 superconducting magnet power supply. The steel can on the right is the cryostat system.

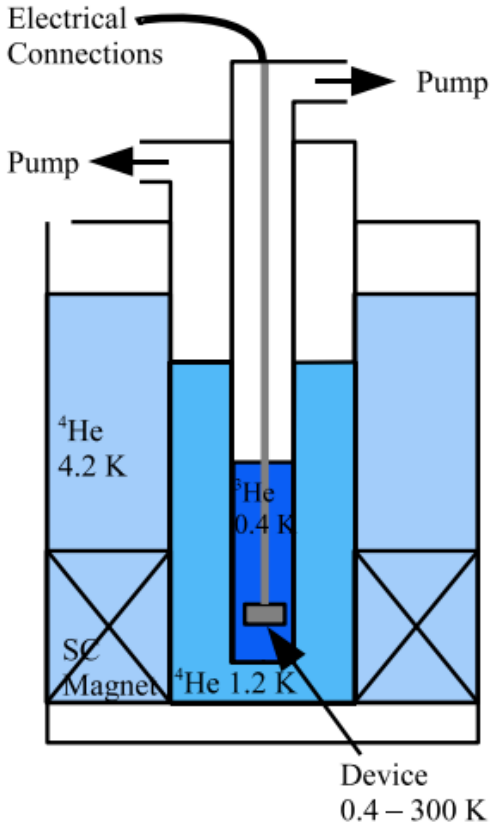

Figure 2.5 Schematics of the ^{3}He cryostat system.

The lock-in amplifiers are utilized for both sourcing current and measuring voltage in order to lower the noise. The lock-in amplifiers used are model SR830 from Stanford Research Systems, model 7265 from EG&G, and model P124A manufactured by Princeton Applied Research. The first two use digital signal processing (DSP) techniques while the third one is an analog instrument. The analog lock-in's signal is digitized by a Keithley (model 2400) voltmeter. Two Yokogama (model GS200) voltage sources are used to supply gate voltages to gate electrodes. The temperature is monitored by a Lakeshore (LS370AC) resistance bridge, which also controls the probe heaters. The external magnet power supply is driven by a Cryomagnetics (model CS-4) or a Kepco (model BOP 20-10D) power supply, where the Kepco is driven by a Keithley (model 2400) source-measure unit in source-voltage mode. All equipment are connected to the computers by general purpose interface bus (GPIB) cables and are synchronized by LabView programs for data.

2.2 References

1. S. V. Aragunathan, “investigation into molecular beam epitaxial growth and characterization of InGaAs structures and InAs superlattices”, Thesis (2014).

Chapter 3. Experiments and theory of an antidot in a mesoscopic channel

In the early 1980s Aharonov and Casher [1] proposed a "dual" effect to the Aharonov-Bohm (AB) effect. The AB effect describes an electrical charge circles around a magnetic flux. The Aharonov-Casher (AC) effect is the interaction between the magnetic moment and an electric field. The quantum phase associated with the AC effect is here referred to as the AC phase, which occurs when a particle with magnetic moment travels in a transverse electric field. It is well known that the integer quantum Hall effect (IQHE) and many related magnetic transport phenomena could be explained invoking the AB effect and phase. Instead of IQHE, the physical phenomena studied in this work occur when replacing the magnetic vector potential with the AC vector potential (defined below). The AC vector potential defines an expression of spin-orbit interaction (SOI), which links magnetic moments and the electrical field. It plays an important role in electrical manipulation of electron spin states (spintronics) and in magnetoelectronics. The work below studies fundamental aspects of the AC vector potential. In two-dimensional systems, the importance of the edge effects for IQHE was shown by Halperin in 1982 [2]. The so-called edge-state picture could help explain many experimental results, quantization, the absence of backscattering, suppression of scattering from one edge of the sample to the other and so on [2, 3]. The edge states induced by the AC vector potential are electromagnetically dual to the IQHE edge states. The AC states are helical, akin, but not necessarily identical, to those characterizing the quantum spin Hall effect (QSHE) state [4-10].

3.1 Theory of the AC edge states

In a thought experiment, we construct the following situation for the 2DES, exposed to a perpendicular magnetic field. Consider an observer in a moving inertial frame, with a velocity relative to the 2DES. According to the Lorentz transformation for electromagnetic fields, the magnetic field for the observer frame could be zero, depending on the relative velocity. As derived in the following part, we map this

observation to the fact that one could observe electrically-induced AC edge states in a mesoscopic narrow-channel geometry.

In geometrically confined systems, the IQHE edge states arise from a broken translational invariance induced by the edge, lifting the degeneracy of the Landau level and leading to propagating chiral edge states. The chirality guarantees that states propagate at the opposite direction at the opposite samples sides. Neither disorder nor roughness at the edge will backscatter the electrons. Thus, the quantization of the Hall conductivity σ_{xy} is very robust and the longitudinal resistivity measured along the current direction vanishes at the plateau region. The QSHE state and its three-dimensional topological insulator analogs [4-9] attracted significant interest for the implications of their topologically protected states. As the IQHE, the QSHE occurs at the edge of a 2D system, but the 1D edge states are correlated with spin [4, 7]. Unlike in the IQHE where spin polarity has no effect on the edge state propagation direction, in the QSHE state of opposite spin counter-propagate on each edge (helical edge states). The current carried by the spin-polarized electrons is protected from the scattering unless time-reversal symmetry is broken, which results in flipping spin and leading to backscattering within one edge [4]. Substituting spin for magnetic moment, such structure can also be realized in the following thought experiment.

As shown in Fig. 3.1a, an observer in the frame $O(x, y, z)$ performs an IQHE experiment in a magnetic field $\boldsymbol{B} = (0, 0, B)$, perpendicular to the x-y plane. To observe the IQHE edge state, a gently varying parabolic confining potential is commonly used to describe the edge profiles [3, 11], $V(x,y) = \frac{1}{2}\omega_p^2 y^2$, where x is parallel to the edge. Therefore, a confinement electric field $\varepsilon = (0, \varepsilon, 0)$ is applied on both sides of the sample, with a y-component linear in y, $\varepsilon = -(\frac{m}{q})\omega_p^2 y$, where q characterizes the carrier charge and m is the mass. The observer in O solves for $H_{AB}\ \boldsymbol{\Psi}(x,y) = E\boldsymbol{\Psi}(x,y)$ with:

$$H_{AB} = \frac{1}{2m}(\boldsymbol{p} - q\boldsymbol{A})^2 + \frac{1}{2}\omega_p^2 y^2 \tag{3.1}$$

where $\boldsymbol{A}$ denotes the vector potential, for instance in the gauge $\boldsymbol{A} = \frac{1}{2}\boldsymbol{B} \times \boldsymbol{r}$ with $\boldsymbol{r}$ in the *x*-*y* plane. The obtained $\boldsymbol{\Psi}(x, y)$ describes the known magnetic edge states [3, 11]. We construct a thought experiment in free-space, where Lorentz transformations apply. Broken translational invariance in crystalline solids restricts our thought experiment to free-space. We note that the Hamiltonian in Eq. 3.1 can, at least in principle, be constructed in free-space, without referring to solids. Also IQHE phenomena can, again at least in principle, be observed in free-space if the proper edge potential profile can be constructed. In the free-space thought experiment, another observer in the frame *O'(x, y, z)* travels at a speed $\boldsymbol{v} = \mathrm{c}^2(\varepsilon \times \mathrm{B})/\varepsilon^2$ in x direction relative to *O* (Fig. 3.1b), where *c* is the speed of the light. Assuming q > 0, in the thought experiment, *O'* follows the counter-clockwise path since $v = -c^2\, B/\varepsilon$ for $y > 0$ and $v = c^2\, B/\varepsilon$ for $y < 0$ (the small segments parallel to the x-axis at the sample ends can be readily included without altering the conclusions below). According to the Lorentz transformation, with the given *v*, the derived *ε*'-field and the *B*'-field in *O'* are given by the following values: *B'* = (0, 0, 0) and $\varepsilon' = (0, \varepsilon\sqrt{(1 - (\frac{v}{c})^2}), 0)$. Then what can the observer see without the magnetic field in *O'* while in *O* the IQHE edge states are observed? The question is not trivial since in *O* the conductance is quantized in terms of a topologically protected Chern number [14, 15, 9], and a corresponding topological protection is reasonably expected in some form under the Lorentz transformation. Thus edge phenomena should also be observed for the moving observer, which will be shown in the following paragraph. In the thought experiment, the observer *O'* will perceive a magnetic moment $\boldsymbol{\mu} = \frac{1}{2}q\boldsymbol{r} \times \boldsymbol{v}$ since the charge *q* is moving at a speed *v,* which also produce a magnetic field $\boldsymbol{B} = (1/c^2)\, \boldsymbol{v} \times \boldsymbol{\varepsilon}$. Given such magnetic field, a magnetic vector potential is introduced as follows: $q\boldsymbol{A} = (1/c^2)\, \boldsymbol{\mu} \times \boldsymbol{\varepsilon}$. The observer hence solves for $H_{AC}\psi(x, y) = E\psi(x, y)$ with:

$$H_{AC} = \frac{1}{2m}\,(\boldsymbol{p} - \frac{1}{c^2}\,\boldsymbol{\mu} \times \boldsymbol{\varepsilon})^2 + \frac{1}{2}\omega_p^2 y^2 \tag{3.2}$$

We drop the primes for each notation. In the Eq. 3.2 the Aharonov-Casher (AC) vector potential $1/c^2\, \boldsymbol{\mu} \times \boldsymbol{\varepsilon}$ is purely generated by an electric field. Whereas the Aharonov-Bohm (AB) effect [16] describes the phase accumulated by a charged particle along a

path through a magnetic flux, its electromagnetic dual, the AC effect [1] describes the phase accumulated by a magnetic moment along a path in an electric field. Fig. 3.1c schematically shows the duality [17] in the interferometric ring geometries, which provide the possibility to detect the effects in mesoscopic experiments. Fig. 3.2 is an image of a ring for the measurement of the AB effect. The ring was fabricated in an InGaAs/InAlAs semiconductor heterostructure by electron beam lithography and reactive ion etching. The diameter of the ring is 700 nm. The darker areas in the picture were etched away to form constrictions for electrons. The white lines indicate the electronically conducting path through the ring as depicted in Fig. 3.2, illustrating the correspondence with Fig. 3.1c (right). The AB quantum phase originates in $\boldsymbol{B}$, which creates a magnetic flux through the ring. The interference pattern is measurable at low-temperature. Experimental examples will be presented below. The AC phase shift was experimentally observed with a neutron beam interferometry for the first time [18]. In the solid-state the similarity of the AC effect to the materials property of SOI has led to experiments [19-22] and theoretical work [23-25]. Expressions of the duality based on the Dirac equation were presented in Ref. 26. The Landau-like levels induced by the AC vector potential for various profiles of ε were described in Ref. 27.

In the thought experiment, both the travel path and velocity of *O'* seem specific, but the main point also applies to general situations. Concerning the path, the expression of H_{AC} is the same for all edges if the observer *O'* moves at the same speed $\boldsymbol{v}$. The conclusions below will hence be valid for all edges along the entire perimeter. Concerning the magnitude $v = -c^2 B/\varepsilon$, it was chosen to yield a pure electric field in the frame *O'*. As a result, there are two correspondent phenomena: H_{AB} describing q in applied $\boldsymbol{B}$ and H_{AC} describing a magnet moment μ in applied $\boldsymbol{\varepsilon}$. Both H_{AB} and H_{AC} can be solved independently regardless of the inertial frames. An intermediate velocity will yield various ratios of perpendicular ε and B. It is noted that the applied mixed ε and B also generate non-trivial edge states, although it will not be discussed in the thesis.

(a) (b)

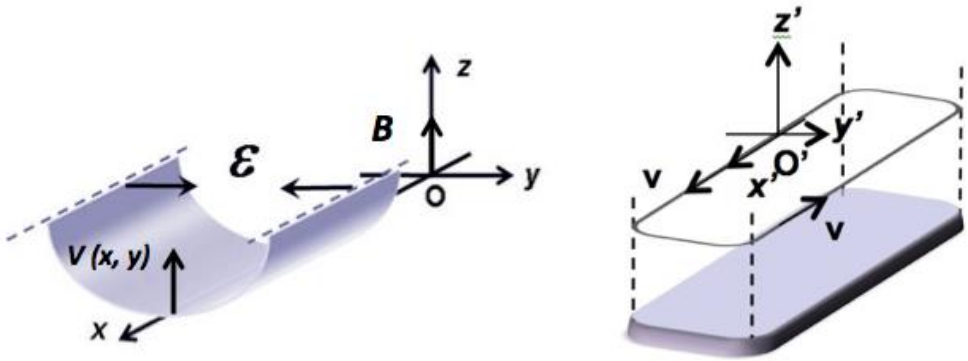

(c)

Figure 3.1 (a) The wire in which the IQHE is set up, with parabolic potential at the edges, and coordinate frame O. (b) The coordinate frame O', and the schematic trajectory with velocity v of the moving observer in the thought experiment. (c) The duality between the AB effect induced by qA and the AC effect induced by $(1/c^2)$ $\boldsymbol{\mu} \times \boldsymbol{\varepsilon}$, illustrated by interferometric ring geometries.

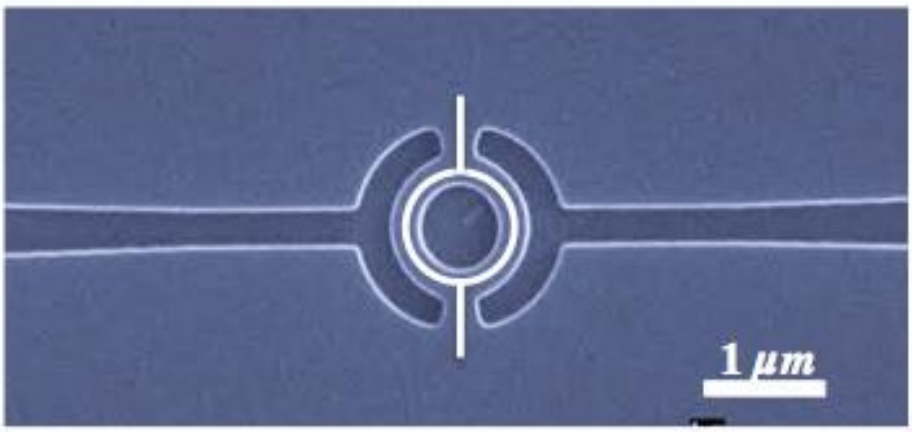

Figure 3.2 SEM micrograph of an experimental realization, by electron-beam lithography and reactive ion etching, of a ring for the measurement of the AB effect in an InGaAs/InAlAs semiconductor heterostructure. The electronically conducting path through the ring is schematically indicated by fine lines. The darker areas represent etched regions, forming barriers for the electrons. The ring has average diameter of 700 nm, and lithographic arm width of 300 nm.

In order to solve the Eq. 3.2, we assume that $\boldsymbol{\mu}$ only has a z component for convenience, such that $\boldsymbol{\mu} = (0, 0, \mu_z)$, which is not strictly necessary since only the product $\boldsymbol{\mu} \times \boldsymbol{\varepsilon}$ matters. We introduce $\omega_A = \frac{\mu_z \omega_p^2 \varepsilon}{(qc)^2} = \frac{1}{2}\omega_p \left(\frac{\mu_z}{\mu_B}\right)\left(\hbar \frac{\omega_p}{mc^2}\right)$ with μ_B the Bohr magneton. It is noted that ω_A is equivalent to the cyclotron ω_C in a magnetic field. The eigenstate of the H_{AC} can be written as $\Psi(x, y) = (\frac{1}{\mathrm{L}})^2 e^{ikx}\zeta(y)$, where L is the length of the sample, k is the electron momentum in the x-direction and $\zeta(y)$ is the eigenfunction of the one-dimensional problem of Eq. 3.3:

$$\left[\frac{1}{2m}\,(\hbar k - m\omega_A y)^2 + \frac{p_y^2}{2m} + \frac{1}{2}\omega_p^2 y^2\right]\zeta(y) = E\zeta(y) \tag{3.3}$$

which can be rewritten as a harmonic oscillator shifted in y in the same way as for edges states in the IQHE [3, 11] :

$$\left[\lambda\frac{\hbar^2k^2}{2m}+\frac{p_y^2}{2m}+\frac{1}{2}m\Omega^2(y-\eta k)^2\right]\zeta(y)=E\zeta(y) \tag{3.4}$$

with $\lambda=\frac{\omega_p^2}{\omega_p^2+\omega_A^2}, \Omega=(\omega_p^2+\omega_A^2)^{1/2}$ and $\eta=h\frac{\omega_A}{[m(\omega_p^2+\omega_A^2)]}$. The eigenvalues are $E_{n,k}=\frac{\lambda(\hbar^2k^2)}{2m}+\hbar\Omega\left(n+\frac{1}{2}\right)$, and the corresponding eigenfunctions $\zeta_{nk}(y)=e^{-\frac{q^2}{2}}H_n(q)$ with $q=y-\eta k$ and with $H_n(q)$ the n^{th} Hermite polynomial. The wavefunction is centered at $y_c=\eta k$. Spatial separation in the context of spin accumulation at the boundaries is also discussed in the context of presumed confinement-induced SOI [12, 28, 29] (*cfr* below) or in the context of quantized magnetization transport [30]. The expected value of the electron velocity along the edge for the eigenstate is described as:

$$v_x=\langle\Psi(x,y)\left|\frac{1}{m}(\hbar k-m\omega_A y)\right|\Psi(x,y)\rangle=\left(\frac{1}{\hbar}\right)\left(\frac{dE_{n,k}}{dk}\right)=\lambda\left(\frac{\hbar k}{m}\right) \tag{3.5}$$

Hence, both the velocity and the position y_c are proportional to k. However, y_c also depends on μ_z via ω_A. The edge states are "spin filtered" compared to IQHE, and are no longer chiral. At the same edge, electrons with opposite spin propagate in the opposite directions as illustrated in Fig. 3.3a. The energy dispersion close the edge is schematically depicted in Fig. 3.3b. The Landau level $E_{n,k}$ is labeled by *n* and the Fermi energy cuts through energy bands at their respective locations y_c, with higher *n* corresponding to locations further to the edge. In the bulk, the $E_{n,k}$forms a gap in analogy with the Landau level in IQHE. Eqs. 3.2-3.4 apply for an arbitrary μ and in particular apply for the moment from a particle of spin ½. In that case, $\mu_z > 0$ and $\mu_z < 0$ are naturally identified with the two projections of the spin along the quantization axis [25, 31]. Supposing the spin to be ½, after solving the Eqs. 3.2-3.4, one can conclude that the quantum transport is dominated by the helical edge states, as depicted in Fig. 3.3a; the spin and the momentum are locked to each other. The edge states of the QSHE are also helical based on the projection of the spin along *z*-direction [4, 6]. Backscattering at one edge in Fig. 3.3a has to be accompanied by a spin-flip process.. Backscattering is suppressed as the temperature T → 0. Thus the physical picture closely parallels the QSHE and particularly the IQHE, and a similar reasoning emerges regarding measurable

quantities [4]. The helical edge states here arise in a simple mesoscopic wire with parabolic confinement potential, under the action of AC vector potential, and do not require the special band structure under which the QSHE was so far described [4-9]. In similarity to the IQHE, the Hamiltonian in Eq. 3.2 breaks time-reversal symmetry, but, due to the parabolic potential, maintains spatial inversion symmetry. It is thus expected that the resulting edge states will show similarities to the edge states in the IQHE.

(a) (b)

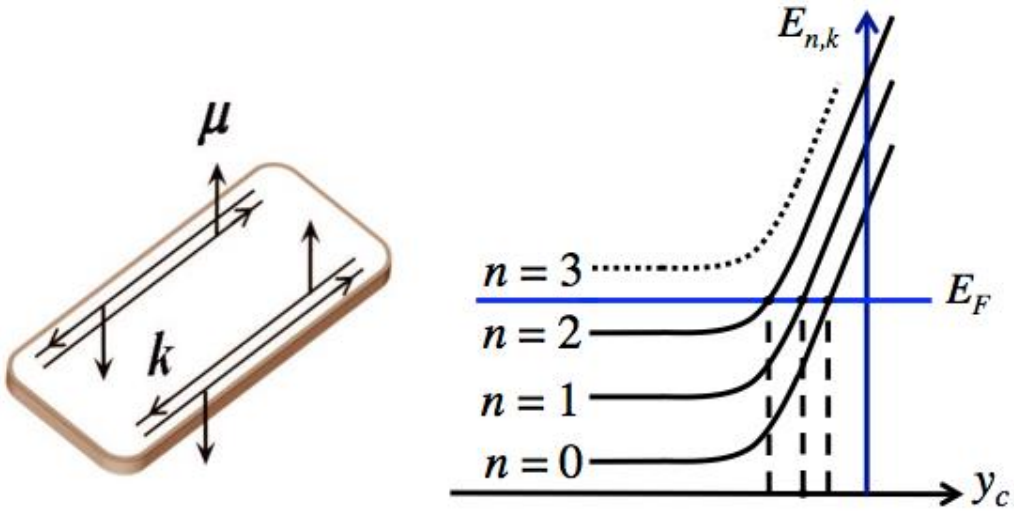

Figure 3.3 (a) Schematic depiction of the helical edge states induced by the AC vector potential. If at a given edge the signs of k and μz are changed simultaneously, the location of the edge state does not change. Counterpropagating states of opposite μz but same n are in fact superposed. (b) Schematic depiction of $E_{n,k}$ as function of the wave function center point y_c. As in the IQHE, propagating states (labeled by n, k and here also μ_z) exist at y-coordinates where E_F intersects $E_{n,k}$.

The electric field $\boldsymbol{\varepsilon}$ plays a significant role since the linearity of ε in y over the sample width leads to an AC vector potential, which has similar effects as the magnetic vector potential of a homogeneous $\boldsymbol{B}$, and the resulting parabolic potential $V(x,y)$ defines the sample's edge. The double role is illustrated by $\Omega = (\omega_p^2 + \omega_A^2)^{1/2}$, where both ω_p and ω_A depend on the existence of the parabolic potential, unlike in IQHE, ω_C is independently created by $\boldsymbol{B}$ equivalent $\Omega = (\omega_p^2 + \omega_A^2)^{1/2}$. The need in Eq. 3.2 to

maintain ε across the sample width indicates a particular relevance for narrow channels, such as encountered in mesoscopic experiments and point-contacts. The energy gap $\hbar\Omega$ leads to an insulating bulk if E_F is located within the gap, while the edges remain metallic (Fig. 3.3b). The gap isolates the edge states and plays an important role in the IQHE and QSHE. We should thus ascertain how deviations from parabolicity in $V(x,y)$ affect the isolation of the helical edge states. To the first order, we find that a perturbation symmetric in y alters the magnitude of the gap but does not qualitatively affect the isolation of edge states. A perturbation asymmetric in y leads to a shift in $E_{n,k}(y_c)$ and can affect the isolation if of sufficient strength, establishing the benefits of a symmetric $V(x,y)$.

Relying on gauge invariance, Laughlin gave a very general argument for integer quantization of $\sigma_{xy} = ne^2/h$ (n is an integer) in IQHE [10, 33]. The argument can be appreciated in the light of the Maxwell-Faraday expression in Maxwell's equation. By the Faraday law,

$$\boldsymbol{\nabla} \times \boldsymbol{\varepsilon} = -\frac{d\boldsymbol{B}}{dt} \tag{3.6}$$

the change in magnetic flux give us a force on charge ($\oint \boldsymbol{F_e} \cdot dl = -e\frac{d\Phi_B}{dt}$), which means a temporal change in magnetic flux by the flux quantum h/e creates a current corresponding to the transport of a unit charge e. Thus the conductance is an integer multiple of e^2/h.

Assuming constant μ, we find that the AC cross line integral of $\boldsymbol{\varepsilon}$ ("AC flux") through Laughlin's cylinder is quantized as:

$$\frac{1}{c^2}\,\boldsymbol{\mu} \cdot \oint \boldsymbol{\varepsilon} \times dl = n2\pi\hbar \tag{3.7}$$

with n an integer. The role of e is assumed by the projection of $\boldsymbol{\mu}$ normal to the plane of $\boldsymbol{\varepsilon}$ (*cfr* Fig 3.1c), μ_n. An easy calculation from Eq. 3.7 shows that the cross line integral of $\boldsymbol{\varepsilon}$ is quantized in units of c^2h/μ_n and hence the role of the flux quantum h/e goes to c^2h/μ_n. The force on a magnetic moment can be expressed as [33]:

$$F_\mu = \nabla(\boldsymbol{\mu} \cdot \boldsymbol{B}) - \frac{1}{c^2}\frac{d}{dt}\,\boldsymbol{\mu} \times \boldsymbol{\varepsilon} \tag{3.8}$$

In analogy to the Maxwell-Faraday expression, the line integral of the force on $\boldsymbol{\mu}$ is expected to equal the temporal change in the cross line integral of $\boldsymbol{\varepsilon}$ in Eq. 3.7. Hence we expect that a transport of a magnetic moment μ_n in response to a temporal change in the cross line integral by the quantum c^2h/μ_n. The relevant analog of conductivity is quantized in μ_n^2/h.

The quantization of $\sigma_{xy} = e^2/h$ in the IQHE is in the dual effect replaced by quantized magnetization transport (see also Refs. 4 and 30). However, unlike e, $\mu_n$is not universal constant, since values for μ is related to interactions in the solid-state as well as for elementary particles. Furthermore, in contrast to charge, magnetization is not a strictly conserved quantity. Thus, while the quantization is expected to occur, universal values are not anticipated. In the broadest terms, we recognize that the AC vector potential, when transformed from the magnetic vector potential, introduces phenomena at the edge of a narrow channel.

Now we rephrase the results from Eqs. 3.2-3.4 in terms of SOI. The SOI Hamiltonian can be written as $H_{SO} = \beta\boldsymbol{\sigma} \cdot (\boldsymbol{k} \times \boldsymbol{\varepsilon})$, where $\boldsymbol{\sigma}$ is the vector of the Pauli matrices, $\boldsymbol{\varepsilon}$ is identified with the in-plane confinement electric field [12, 28, 34]. It is important to remember that if the system described by the wavefunction is confined by this electric field only, then the electric field value integrated over the wavefunction will be zero (Ehrenfest theorem), and no SOI effect is expected [37, and other papers by R. Winkler]. For example, the lateral electric field profile experienced by a wavefunction straddling the entire width of a quantum point contact is not expected to lead to SOI. The electric field profile and the wavefunction envisaged in this thesis are such that the electric field does not integrate to zero over the wavefunction, a situation that has a precedent in the edge states of the IQHE. With an electric field of the form $\varepsilon = -(\frac{m}{q})\omega_p^2 y$ in y direction, $\boldsymbol{k}$ parallel to x direction and the projection of spin along z, the SOI Hamiltonian can be rewritten as $H_{SO} = -\hbar\,\boldsymbol{k}\omega_S y$, which defines ω_S, with a role equivalent to ω_A above. In analogy to Eq.3.3, the transverse function of $\zeta(y)$ follows:

$$\left[\frac{\hbar^2k^2}{2m} - \hbar k\omega_S y + \frac{p_y^2}{2m} + \frac{1}{2}\omega_p^2 y^2\right]\zeta(y) = E\zeta(y) \tag{3.9}$$

By introducing the parameter $\omega'^2_p = \left(\omega_p^2 - \omega_S^2\right)$, the Eq. 3.9 can be rewritten in the following form mathematically identical to Eq. 3.3:

$$\left[\frac{1}{2m}(\hbar k - m\omega_S y)^2 + \frac{p_y^2}{2m} + \frac{1}{2}\omega'^2_p y^2\right]\zeta(y) = E\zeta(y). \tag{3.10}$$

As a shifted harmonic oscillator, the energy is expressed as $E_{n,k} = \lambda'(\hbar^2k^2)/(2m) + \hbar\Omega'\left(n + \frac{1}{2}\right)$ with $\lambda' = \frac{\omega'^2_p}{\omega'^2_p + \omega_S^2}$, and $\Omega' = (\omega'^2_p + \omega_S^2)^{1/2}$. The transverse wavefunction becomes $\zeta_{nk}(y) = e^{-\frac{q^2}{2}}H_n(q)$ with $q = y - \eta'k$ where $\eta' = \hbar\frac{\omega_S}{\left[\mathrm{m}\left(\omega'^2_p + \omega_S^2\right)\right]}$. Hence $\zeta_{nk}(y)$ is now centered at $y = \eta'k$. Since Eq. 3.10 is completely identical to Eq. 3.3, spatially separated helical edge states would be encountered. The helical edge states induced by H_{SO} are thus equivalent to the AC edge states. The electric field $\boldsymbol{\varepsilon}$ at edges of a mesoscopic channel would have a more complicated form rather than a parabolic $V(x,y)$ with an in-plane $\boldsymbol{\varepsilon}$ [13, 35]. For instance, a z-component of $\boldsymbol{\varepsilon}$ that depends on y, $\varepsilon_z(y)$, likely exists in these systems, in addition to the in-plane component of $\boldsymbol{\varepsilon}$. As mentioned above however, only $\boldsymbol{\mu} \times \boldsymbol{\varepsilon}$ matters, and with Bychkov-Rashba SOI [36, 37] aligning spin perpendicular to $\boldsymbol{k}$ and to $\boldsymbol{z}$, $\varepsilon_z(y)$ can then lead to a term analogous to $-\hbar k\omega_S y$. We conclude that in mesoscopic channels, either the y- or inhomogeneous z-component of $\boldsymbol{\varepsilon}$ can yield helical edge states, with implications for transport phenomena [38].

Next we outline experimental challenges to observe the helical states from Eqs. 3.2-3.4. We assume that the observer uses the electron spin for μ and the confinement field for $\boldsymbol{\varepsilon}$. As described above for SOI, the term $\mu \times \boldsymbol{\varepsilon}$ can either arise from the projections of spin along z (via ε_y) or along y (via $\varepsilon_z(y)$). To maximize μ and minimize the effective c, we consider quasi-relativistic [39] narrow-gap semiconductors with large electron g-factors (g), InGaAs [31], InAs [40] or InSb [41–43]. The band structure implies a momentum *vs* energy response differing from that in vacuum, determining the electron dynamics under electromagnetic fields. According to the two-band model, the effective light speed c is

approximately equal to $(E_g/2m^*)^{1/2}$, where E_g are the bandgap and m^* the effective mass at the Γ-point [39]. For InGaAs, InAs and InSb it is found that $c \approx 1.2 \times 10^6$ m/s, about 250 times lower than the vacuum value. The magnetic moment is considered to be $\mu = \frac{1}{2}\mu_B$. Using InAs as an example, at the Γ-point, m^* is equal to $0.024m_e$ with m_e the free electron. In the 2DES, the typical value for the carrier charge density is $n_s \approx 10^{12}$ cm^{-2} which results in Fermi energy E_F = 83 meV. To obtain a value for ω_p, we use E_F as the approximate classical turning point of $V(x,y)$ and assume a depletion layer width of 0.15 μm at the edge, within the range of values encountered in 2D system (depletion layers in InSb 2DESs [43, 44] are wider than in InAs 2DESs [22], likely due to the accumulation layer present at InAs surfaces [45]). We find $\varepsilon \approx 10^6$ V/m (similar values of ε, about an order of magnitude below breakdown, are typical in semiconductor heterostructures, justifying the approach). With these values we find $\hbar\omega_A \approx 0.01$ meV, corresponding to 0.13 K. It is equivalent to apply a few mT in a GaAs 2DES IQHE experiment to obtain such small energy gap, which provides challenges for experiments closely copying the standard IQHE geometries. A typical geometry is the interferometric mesosocopic ring as mention above where the difference between AC phases of opposite spin states traveling clockwise and counterclockwise around the ring generates mesoscopic quantum interference effects that can be observed. Also, the dual effect indicates quantized magnetization transport. Since the magnetic moment is not a fundamental constant compared to charge, it is difficult to measure the magnetization transport directly. From Eq. 3.2, oscillations should also be observed in the magnetotransport similar to Shubnikov-de Haas effect. In the edge state regime, it is possible to perform measurements based on altering the edge state structure via side gates, or using applied magnetic fields to align $\boldsymbol{\mu}$ parallel to $\boldsymbol{\varepsilon}$.

3.2 Experiment & Results discussion

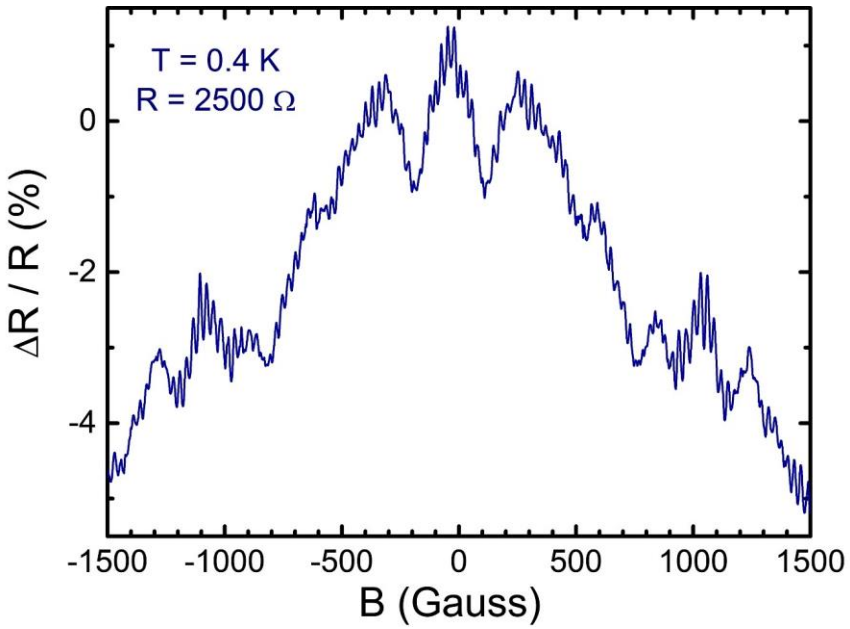

Figure 3.4 Magnetoresistance $R(B)$ at T = 0.4 K due to AB oscillations in a single ring fabricated on an InGaAs 2DES [10, 46].

Recent attempts in spintronics to control the spin for quantum information processing render experiments to test the reality of AC edge states compelling, and we now extend the idea to the AC effect in the 2DES. In the mesoscopic ring, as illustrated in Fig. 3.2 with the diameter 1.4 μm and lithographic arm width 300 nm, the phase difference between the wavefunctions is $-\left(\frac{e}{\hbar}\right)Br^2$ in the presence of perpendicular magnetic field B, where r is the radius of the path. The change of the magnetic field leads to the constructive and destructive interference, which manifest itself in an oscillation of the conductance as a function of B with a magnetic flux period h/e. Such phenomenon is known as AB oscillations [10, 46, 47]. Fig. 3.4 shows the oscillations at low magnetic field B < 0.3 T in the InGaAs 2DES single ring [10, 46]. The InGaAs/InAlAs heterostructure material is the same as described in Chapter 2. The observed period ΔB = 2.9 mT corresponding to a circular area with a radius 675 nm, which is in excellent agreement with the expected h/e flux periodicity. The quasi-periodic background is representative of universal conductance fluctuations in quantum-coherent mesoscopic devices. Since the material has high electron density $n = 9\times10^{15}$ m^{-2} and high mobility

$\mu = 5.9$ m^2/Vs at $T = 0.4$ K, the electron quantum phase coherence length reaches several μm at T = 0.4 K, allowing phase-coherent measurements. On the other hand, the heterostructure is asymmetrically doped, where the Bychkov-Rashba SOI [37, 38] is dominant. Similar but electromagnetically dual interferometric measurements in semiconductor devices form the basis for the experimental pursuit of AC phases and AC edge states.

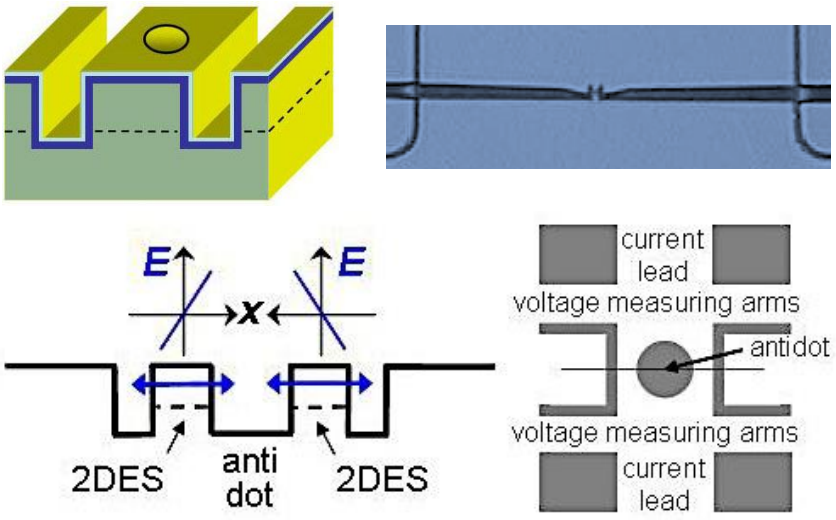

Figure 3.5 Top right: Photograph of a representative antidot (ø 300 nm) in a channel (1 µm width) sample. Top left: Schematic of quantum antidot samples. Bottom right: Schematic of top view of the antidot. Etched regions are dark. Voltage measurement arms and current leads are connected to electrical contacts. Bottom left: Horizontal cross-section through the sample, schematically showing conducting 2DES regions and in-plane confinement ε.

In our experiment, we fabricated a quantum antidot (QAD, an etched disc inaccessible for electrons, diameter 300 nm) with the same material as the sample in Fig. 3.2 in a narrow and short channel (width and length 1.0 µm) [48-52]. The InGaAs/InAlAs heterostructure material is also the same as described in Chapter 2. The details are illustrated in Fig. 3.5. With this geometry, we expect to access AC phases and AC edge states. The sample was measured at $T = 1.2$ K in a B tilted at an angle to the 2DES normal [10]. The approximate profile of $\boldsymbol{\varepsilon}$ for the QAD sample is depicted in Fig. 3.5 (bottom left): we can assume a parabolic confinement potential (linear $\boldsymbol{\varepsilon}$) in the channels on the side of the QAD, and a

decaying $\boldsymbol{\varepsilon}$ in the direction of the current leads (Fig. 3.5, bottom right). In Fig. 3.6 magnetoresistance as a function of the normal component of $\boldsymbol{B}$, $B_n = B \sin[\theta]$ is shown for varying the angle θ between the $\boldsymbol{B}$ and the 2DES plane from $\theta = 0^o$ (in-plane, $\boldsymbol{B}$ // measurement current) to $\theta = 90^o$ ($\boldsymbol{B} \perp$ 2DES). Based on the Hall measurement as shown in Fig. 3.6a, we can find out much more accurate angles by fitting the slope of $\sin[\theta]$ since V_H is proportional to B_n. Multiple B_n periodicities of *AB*-type oscillations (Fig. 3.6b) appear at low *B* due to closed paths less well defined than on ring geometries. When varying θ, fine structure appears in the magnetoresistance when the in-plane component of $\boldsymbol{B}$, $B_{//} = \cos[\theta]$, is appreciable (e.g. $\theta < 48^o$, Fig. 3.6b), in the moderate range of B_n studied (0.5 T). With the applied $B_{//}$, the time reversal symmetry was broken as a result of Zeeman splitting, and also the effectiveness of spin-orbit interaction grows if $B_{//}$ increases [53-55]. In our experiment, these effects are small due to the comparatively strong Rashba SOI [36, 37]. Indeed, Rashba SOI corresponds to an in-plane effective $B \approx 3$ T, while $B < 0.5$ T. Varying θ changes the total $\boldsymbol{B}$ experienced by the electrons (applied $\boldsymbol{B}$ plus effective in-plane $\boldsymbol{B}$ from Rashba SOI) and hence a rotation in the spin precession axis. This leads to a rotation in μ at each point along the paths and a change in $\left(\frac{1}{c^2}\right)\boldsymbol{\mu} \times \boldsymbol{\varepsilon}$, integrated over the interfering paths. The rotation is small ($<<\tan^{-1}[\frac{0.5}{3}] \approx 10^o$) at any path along the path, limited by the mostly in-plane spin direction and the moderate $B_{//}$. Effects of the AC phase are hence expected to be moderate and smoothly varying in θ. Indeed, moderate amplitude change is observed in Fig. 6b. Yet, the fine structure at $\theta = 12^o$ cannot be ascribed to the AC phase between AC edge states formed on opposite edges of each of the two narrow side channels formed between the channel walls and the QAD. When the resonant tunneling condition is fulfilled, communication is established between the AC edge states on opposite sides of the channel, resulting in a breakdown in the absence of backscattering and a measurable resistance change. The mT spacing for the fine structure in Fig. 3.6b is consistent with the expected approximate energy spacing between AC edge states, as derived above. Moreover, samples without the central QAD do not show fine structures, in agreement with the hypothesis that the QAD forms a resonant island, which allows detection of AC edge states. We have also investigated channels with 5 QADs in series (Fig. 3.7), and

could not identify fine structure since averaging over variations in QAD diameter reduces the resonance peaks.

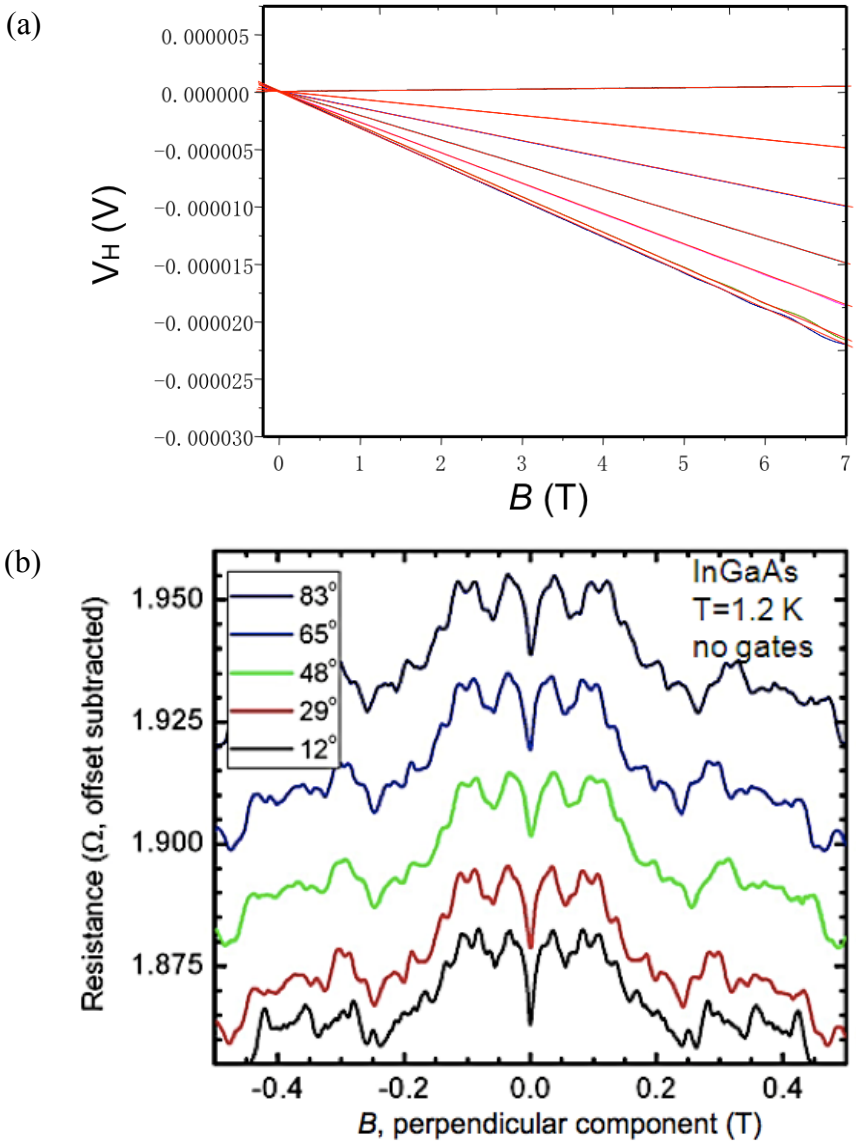

Figure 3.6 (a) θ extracted from the Hall effect. (b) Angular dependence of the magnetoresistance vs $B_{\perp}$ of a narrow InGaAs channel with a quantum antidot at 1.2 K (insert: θ values).

In summary, we address Aharonov-Casher edge states in a narrow channel. The direction of electron spin of the helical edge states is locked to perpendicular to the electron momentum *k*, which is similar to the edge states in the recently-described QSHE. It was also found that the AC flux could lead to interference phenomena as the AB flux. Other sets of closely-related effects may also exist due to the duality of the AB effect and AC effect. Beyond fundamental interest, the Aharonov-Casher phenomena may also provide a promising way to electrically manipulation of spin and magnetic moments in magnetoelectronics.

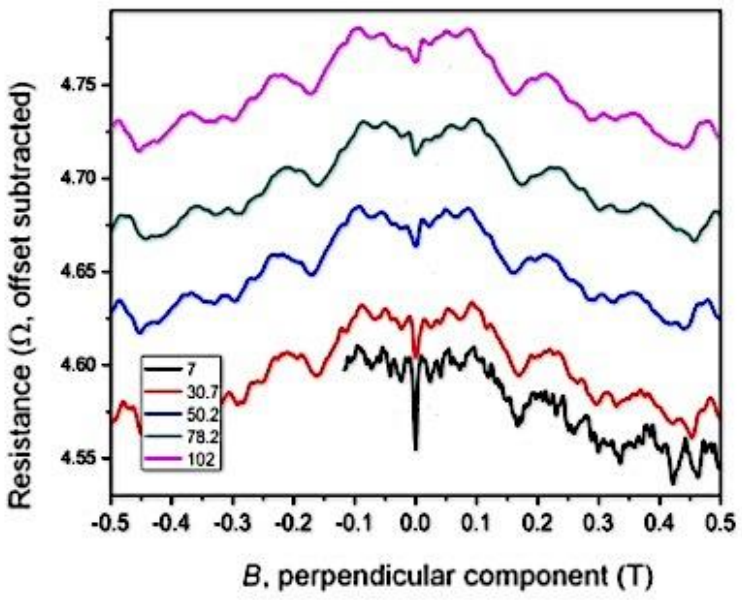

Figure 3.7 Angular dependence of the magnetoresistance vs $B_{\perp}$ of a narrow InGaAs channel with a quantum antidot at 1.2 K (insert: θ values).

3.3 References

1. Y. Aharonov, A. Casher, *Phys. Rev. Lett.* 53, 319 (1984).

2. B. Halperin, Phys. Rev. Lett. **63**, 380 (1989).

3. A. H. MacDonald, and P. Streda, Phys. Rev. B 29, 1616 (1984).

4. C. L. Kane, and E. J. Mele, Phys. Rev. Lett. 95, 226801 (2005).

5. B. A. Bernevig, T. A. Hughes, and S. C. Zhang, Science 314, 1757 (2006).

6. M. Koenig, S. Wiedemann, C. Brne, A. Roth, H. Buhmann, L. W. Molenkamp, X. L. Qi, and S. C. Zhang, Science 318, 766 (2007).

7. L. Fu, C. L. Kane, and E. J. Mele, Phys. Rev. Lett. 98, 106803 (2007).

8. J. E. Moore, and L. Balents, Phys. Rev. B 75, 121306(R) (2007).

9. (a) for reviews, see M. Koenig, H. Buhmann, L. W. Molenkamp, T. Hughes, C. X. Liu, X. L. Qi, and S. C. Zhang, J. Phys. Soc. Jpn. 77, 031007 (2008); (b) M. Z. Hasan and C. L. Kane, Rev. Mod. Phys. 82, 3045 (2010).

10. L. Xu, Shaola Ren, and J. J. Heremans, Integr. Ferroelectr. 131, 36–46 (2011)

11. W. Zawadzki, Springer Series in Solid-State Sciences Vol. 87, High magnetic fields in semiconductor physics II, ed. G. Landwehr (Springer-Verlag Berlin Heidelberg, 1989).

12. K. Hattori, and H. Okamoto, Phys. Rev. B 74, 155321 (2006).

13. J. H. Hsiao, K. M. Liu, S. Y. Hsu, and T. M. Hong, Phys. Rev. B 79, 033304 (2009).

14. D. J. Thouless, M. Kohmoto, M. P. Nightingale, and M. den Nijs, Phys. Rev. Lett. 49, 405 (1982).

15. Y. Hatsugai, Phys. Rev. Lett. 71, 3697 (1993).

16. Y. Aharonov, and D. Bohm, Phys. Rev. 115, 485 (1959).

17. R. Hagen, Phys. Rev. Lett. 64, 2347 (1990).

18. A. Cimmino, G. I. Opat, A. G. Klein, H. Kaiser, S. A. Werner, M. Arif, and R. Clothier, Phys. Rev. Lett. 63, 380 (1989).

19. Z Zhu, Y Wang, K Xia, XC Xie, Z Ma, Phys. Rev. B 76, 125311 (2007).

20. T. Bergsten, T. Kobayashi, Y. Sekine, and J. Nitta, Phys. Rev. Lett. 97, 196803 (2006).

21. M. Koenig, A. Tschetschetkin, E. M. Hankiewicz, J. Sinova, V. Hock, V. Daumer, M. Schaefer, C. R. Becker, H. Buhmann, and L. W. Molenkamp, Phys. Rev. Lett. 96, 076804 (2006).

22. R. B. Lillianfeld, R. L. Kallaher, J. J. Heremans, Hong Chen, N. Goel, S. J. Chung, M. B. Santos, W. Van Roy, and G. Borghs, Physics Procedia 3, 1231 (2010).

23. H. Mathur, and A. D. Stone, Phys. Rev. Lett. 68, 2964 (1992).

24. A. V. Balatsky, and B. L. Altshuler, Phys. Rev. Lett. 70, 1678 (1993).

25. X. F. Wang, and P. Vasilopoulos, Phys. Rev. B 72, 165336 (2005).

26. Ya. I. Azimov, and R. M. Ryndin, JETP Lett. 61, 454 (1995).

27. S. Bruce, J. Phys. A 38, 6999 (2005).

28. Y. Jiang, and L. Hu, Phys. Rev. B 74, 075302 (2006).

29. Y. Xing, Q.-f. Sun, L. Tang, and J. Hu, Phys. Rev. B 74, 155313 (2006).

30. F. Meier, and D. Loss, Phys. Rev. Lett. 90, 167204 (2003).

31. M. Kohda, T. Bergsten, and J. Nitta, J. Phys. Soc. Japan 77, 031008 (2008).

32. R. B. Laughlin, Phys. Rev. B 23, 5632 (1981).

33. Y. Aharonov and D. Rohrlich, Quantum paradoxes: quantum theory for the perplexed, Wiley (2005), ISBN 978–3-527–40391-2, chapter 13.4.

34. P. Debray, S. M. S. Rahman, J. Wan, R. S. Newrock, M. Cahay, A. T. Ngo, S. E. Ulloa, S. T. Herbert, M. Muhammad, and M. Johnson, Nature Nanotechnology 4, 759 (2009).

35. J. A. Nixon, J. H. Davies, and H. U. Baranger, Phys. Rev. B 43, 12638 (1991).

36. Y. A. Bychkov, and E. I. Rashba, Journal of Physics C 17, 6039 (1984).

37. R. Winkler, Springer Tracts in Modern Physics Vol. 191, Spin-orbit coupling effects in twodimensional electron and hole systems (Springer-Verlag, Berlin Heidelberg, 2003).

38. A review can be found at: J. Phys.: Condens. Matter 20, No. 16 (2008).

39. W. Zawadzki, S. Klahn, and U. Merkt, Phys. Rev. Lett. 55, 983 (1985).

40. S. Brosig, K. Ensslin, and A. G. Jansen, Phys. Rev. B 61, 13045 (2000).

41. R. L. Kallaher, and J. J. Heremans, Phys. Rev. B 79, 075322 (2009).

42. R. L. Kallaher, J. J. Heremans, N. Goel, S. J. Chung, and M. B. Santos, Phys. Rev. B 81, 075303 (2010).

43. R. L. Kallaher, J. J. Heremans, N. Goel, S. J. Chung, and M. B. Santos, Phys. Rev. B 81, 035335 (2010).

44. Hong Chen, J. J. Heremans, J. A. Peters, N. Goel, S. J. Chung, and M. B. Santos, Appl. Phys. Lett. 86, 032113 (2005).

45. D. C. Tsui, Phys. Rev. B 12, 5739 (1975).

46. S. L. Ren, J. J. Heremans, C. K. Gaspe, S. Vijeyaragunathan, T. D. Mishima and M. B. Santos, J. Phys.: Condens. Matter 25, 435301 (2013)

47. . S. L. Ren, J. J. Heremans, C. K. Gaspe, S. Vijeyaragunathan, T. D. Mishima and M. B. Santos, J. Phys.: Condens. Matter 18, 185801 (2015)

48. J. A. Simmons, H. P. Wei, L. W. Engel, D. C. Tsui and M. Shayegan, Phys. Rev. Lett. 63, 1713 (1993). 47. V. J. Goldman and B. Su, Science 267, 1010 (1995).

49. A. S. Sachrajda, Y. Feng, R. P. Taylor, G. Kirczenow, L. Henning, J. Wang, P. Zawadzki and P. T. Coleridge, Phys. Rev. B 50, 10856 (1994).

50. V. J. Goldman, I. Karakurt, J. Liu and A. Zaslavsky, Phys. Rev. B 64, 085319 (2001).

51. I. Karakurt, V. J. Goldman, J. Liu and A. Zaslavsky, Phys. Rev. Lett. 87, 146801 (2001).

52. V. J. Goldman, J. Liu and A. Zaslavsky, Phys. Rev. B 77, 115328 (2008).

53. F. E. Meijer, A. F. Morpurgo, T. M. Klapwijk, J. Nitta, Phys. Rev. Lett. 94, 186805 (2005).

54. F. E. Meijer, A. F. Morpurgo, T. M. Klapwijk, T. Koga and J. Nitta, Phys. Rev. B 70, 201307 (2004).

55. D. M. Zumbuhl, J. B. Miller, C. M. Marcus, D. Goldhaber-Gordon, J. S. Harris, K. Campman ¨ and A. C. Gossard, Phys. Rev. B 72, 081305R (2005).

Chapter 4. Channel with side-gates, and simulations

As described in Chapter 3, the AC effect, akin to SOI, will lead to helical edge states and contribute interesting transport properties to 2DESs [1]. The AC effect and SOI have attracted attention because of their potential role in coherent spin rotators, spin interference devices, and spin filters [2-5]. The key idea of the above devices is to utilize the fact of the spin procession caused by AC effect or SOI effect. The modulation of the current can be expected by control of either the alignment of the electron's spin or the electric field, which lifts the spin degeneracy [6]. A spin splitting has been attributed to RSOI in narrow gap semiconductor systems [7, 8], which originates from the lack of version symmetry in quantum wells (QWs) [9, 10]. It appears reasonable that the spin splitting should be proportional to the electric field ε and can be tuned by changing the shape of the confining potential via gate voltage. Since the conductivity strongly depends on SOI [11], most studies focus on the conductance as a function of gate electric potential and magnetic field [12, 13]. Koga et al. [4] demonstrated SOI could be controlled with top gate voltage in InGaAs heterostructures. The spin-splitting value Δ_0 at zero-field was there obtained from analyzing weak antilocalization (WAL). In fact, the beat pattern of Shubnikov-de Haas oscillations (SdH) has also been employed to determine value of a splitting Δ [6]. The Δ value deduced from the beating node position is usually different from Δ_0 since Δ includes the effect of the Zeeman spin-splitting at finite fields [4, 14]. The beatinglike patterns can also be evoked by a slight occupation of the second lowest subband [15] or inhomogeneities of the sheet carrier concentration [16-18]. Thus, the WAL measurement can be said to be a more reliable tool for experimental determination of Δ_0 compared to the SdH beating pattern analysis.

In this chapter, we present gated device at different side-gate voltages and find that ε_y (in plan) and ε_z increase approximately linearly with the side-gate voltage. By fitting the WAL curves at different side-gate voltages we extract the corresponding SOI parameter, which confirms that the SOI can be controlled by the side-gate voltage. Controlled here does not necessarily imply created, and a related discussion of confinement electric fields, SOI, and the implications of the Ehrenfest theorem, can already be found in Chapter 3.

Mindful of the implications of the Ehrenfest theorem for SOI, in this chapter we can conclude that side-gate voltages can modify SOI, but cannot conclude which electric field component is responsible.

4.1 Device Design and Fabrication

The $In_{0.64}Ga_{0.36}As/In_{0.45}Al_{0.55}As$ 2DES heterostructure used in this study was grown by molecular-beam epitaxy system on semi-insulating InP (001) substrate. The 10 nm wide $In_{0.64}Ga_{0.36}As$ quantum well is located 50 nm below the surface. Electrons are provided to the well by Si δ-doped layers separated by 18 nm $In_{0.45}Al_{0.55}As$ layer above the well. The InGaAs/InAlAs heterostructure material is the same as described in Chapter 2 with the electron density $N_S \approx 1.0 \times 10^{16}$ m^{-2} and the mobility $\mu \approx 5.9$ m^2/Vs at $T = 0.4$ K. We fabricated a side-gated channel, as seen in Fig. 4.1a, of different width and length based on this heterostructure using electron-beam lithography and inductively coupled plasma reactive ion etching (ICP-RIE). From the lithography, we have the wide channel with width $w_{litho} = 2$ μm and length $L = 4.2$ μm and the narrow channel with width $w_{litho} = 1$ μm and length $L = 1.4$ μm. The voltage applied via side-gates creates a lateral electric field, which contributes to a variable α characterizing the RSOI. In the sections below, the magnitude of α will be extracted from the WAL data and corrected by the effective not the lithographic-channel width w. Magnetotransport across the channel was measured at several side-gate voltages in a small range of magnetic field B perpendicular to the sample using standard low-frequency lock-in techniques at 0.4 K. Measurements of SdH oscillations show that the electron density N_S and the mobility μ are unaffected by the side-gate voltage. But, the effective channel width w is dependent on the magnitude and sign of the side-gate voltage applied. We estimate the effective width w of the channel from the value of the zero-field resistance R_0 according to the simple relationship $R_0 - R_C = L\rho_{2D}/(w_{litho} - w_{dep}) = L\rho_{2D}/w$; where $\rho_{2D} = (1/N_S e\mu)$ is the sheet resistivity of the 2DES, w_{dep} is the average depletion width and R_C is the effective series contact resistance (mostly due to the 2DES regions flanking to the channel). Based on the device geometry, we estimated $R_C \approx 752$ Ω taking into account a sheet resistance of 65 Ω/square. The estimated width w as a function of side-gate voltage V_G is plotted in Fig. 4.1b for both narrow channel and wide channel.

(a)

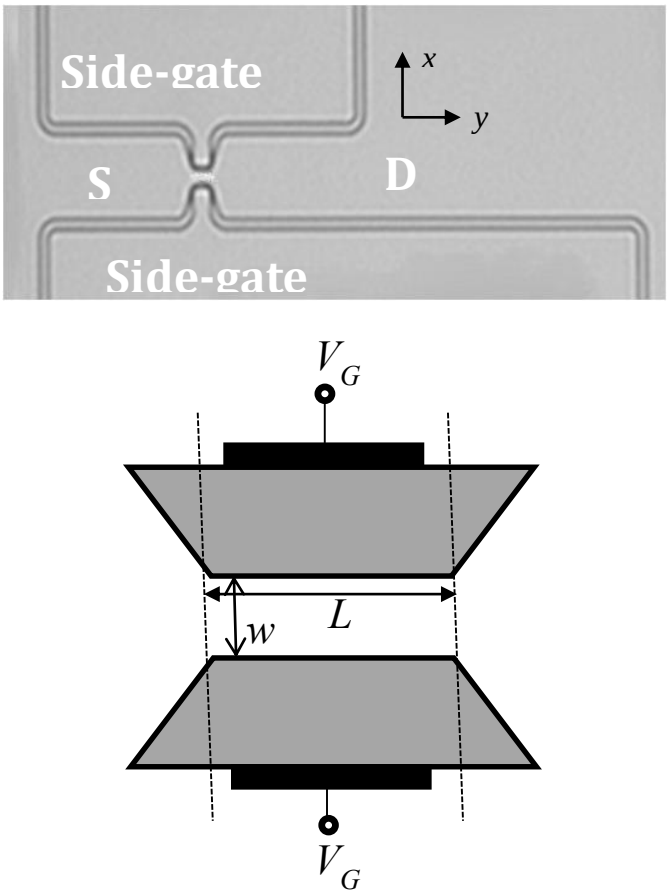

(b)

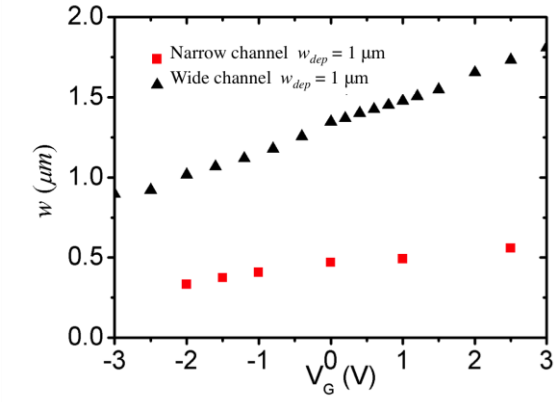

Figure 4.1 Micrograph of a typical side-gated InGaAs channel together with the illustration of the channel area. The grey trapezoidal areas represent the enlarged etched regions. (b) Dependence of w on V_G for both narrow channel and wide channel.

4.2 The electrostatic simulation and theoretical model

In the experiment, the center channel is connected to the same ground as the current return contact and the two side gates were biased with a voltage with respect to that ground. It is reasonable to model the channel as being connected to two capacitors, representing the gaps between channel and side gates, as shown in Fig. 4.2a. If each capacitor has charge +Q (also implying each side gate carries charge +Q), the channel has charge -2Q. We perform a numerical electrostatics simulation, to help us visualize the electric field lines and the vector field. Based on our capacitor model, we ignore the field component along the longitudinal channel direction and substitute side-gates by charged plates to simulate the electrostatics transverse to the channel, namely in a cross-section of the channel device. The dimensions of the narrow channel and the wide channel are illustrated in Fig. 4.2b and Fig. 4.2c, where the green area is air and the blue area is the material. Figure 4.2b shows the choice of coordinate axes, where x runs transverse to the channel's length, and y is normal to the 2DES. We take the charge of the left and the right plates $\sigma_L = \sigma_R = -10^{-3}$ C, and the charge of 2DES in between (i.e. the channel) $\sigma_{2DES} = 2\times10^{-3}$ C. From the simulation, it appears that around the middle of the channel the electric field component $\mathcal{E}_x$ is small and $\mathcal{E}_y$ is large, while at the edges $\mathcal{E}_x$ is large and $\mathcal{E}_y$ small. The magnitude of the total field $\mathcal{E}$ is approximately constant. From the simulation, it is also apparent that the electric field $\mathcal{E}$ is proportional to the density of the charge, which equivalent to mean that $\mathcal{E}$ is linear with the applied side voltage (as expected).

However, to more precisely calculate the electrostatic potential for electrons in the 2DES, we employ a self-consistent Thomas-Fermi-Poisson approach to obtain the distribution of the potential [19-21]. An important theoretical model induced by Glazman *et al.* [22] solved the problem using a purely electrostatic model. They assumed the gates, the donors, and the 2DEG are on the same plane in the z direction. However, they did not consider the electrochemical equilibrium. In another useful model developed by Davies *et al.*, they obtained the analytical solutions with periodic boundary conditions in x and y directions without considering the charge distribution in the 2DES [23]. As depicted in Fig. 4.3a for our system, the right and the left gate are separated from each other by the

channel, the separation distance being $2w$ along the x direction. The distance from the surface to the electron gas is l. This is the distance between the gates at the surface on one hand and 2DES on the other. Yet in our model we ignore this distance and set $l = 0$. The half-space $z < 0$ is fully filled by the semiconductor with dielectric constant ϵ. The total electrostatic potential energy is given by

$$V = V_d + V_H \tag{4.1}$$

where V_H is caused by the voltages V_L and V_R in the absence of the donors and V_d is created by ionized donors which is taken as a form from a frequently used model [19, 21]

$$V_d = -E_0\sqrt{(1 - \frac{x^2}{w^2})}, \qquad E_0 = \frac{2\pi e^2}{\epsilon} N_s w. \tag{4.2}$$

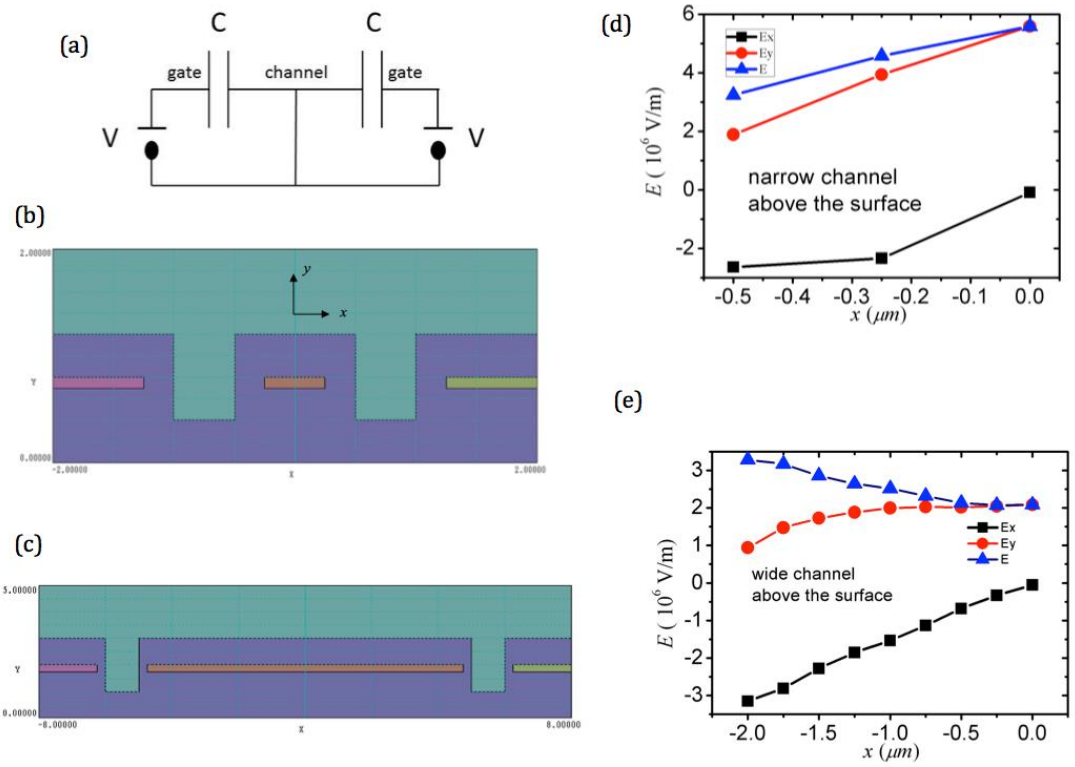

Figure 4.2 (a) Simplified capacitor model for the side-gated device. (b), (c) Model used for simulation for both narrow and wide channel. (d), (e) Simulated electric field components at y = 1 for the narrow channel and y = 2.5 for the wide channel. The field values are not necessarily representative of experiments, and are obtained for the values of test charges mentioned in the text. The field values in fact scale linearly with charge and side-gate voltage values (as expected).

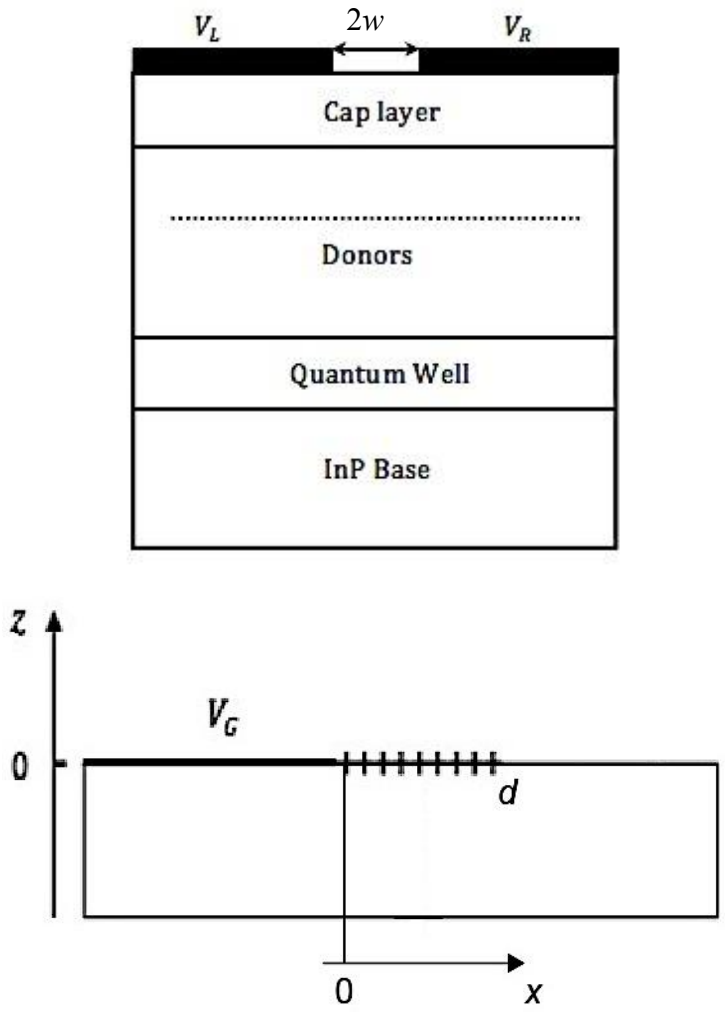

Figure 4.3 Schematic layout of the sample. The gates are deposited on the sample surface, and have a separation 2*w* along *x*-direction. With a negative side-gate voltage, the 2DES is depleted. The depletion width is assumed to be *d*.

To calculate V_H, we consider a 3D model with translational symmetry in y direction (direction longitudinal along the channel), high value of the dielectric constant in the half space $z < 0$ ($\epsilon \gg 1$), and with a charge density concentrated in the $x - y$ plane. The electrostatic potential energy of an electron is $U(x, y) = -e\phi(x, y)$, with ϕ being the electrostatic potential and satisfying the boundary condition

$$U(x, z = 0) = U_0, \quad \text{x} < 0 \tag{4.3}$$

at the gate, where $U_0 = -\text{e}V_G$, and V_G is the applied gate voltage;

$$\left.\frac{dU(x,z)}{dz}\right|_{z\to-0} = -\frac{4\pi e\rho(x)}{\epsilon} \tag{4.4}$$

for the electric displacement field where $\rho(x)$ in units C/m^2 is the total charge density at the surface ($z = 0$), with the positive background electron density n_0 (m^{-2}) subtracting electron density $n_s(x)$ (m^{-2}) in 2DES,

$$\rho(x) = e\big(n_0 - n_s(x)\big) \tag{4.5}$$

For $z \neq 0$, the electrostatic potential should satisfy $\nabla^2 U(x,z) = 0$, so that we can write $U(x,z)$ as the imaginary part

$$U(x,z) = Im\, F(\xi) \tag{4.6}$$

of a holomorphic function F of the complex variable $\xi = x + iz$. As in Ref. 21, the solution is given by

$$U(x) = U_0 - \int_0^\infty dt\ \ln\left|\frac{\sqrt{x}+\sqrt{t}}{\sqrt{x}-\sqrt{t}}\right| \frac{r(t)}{\pi} \tag{4.7}$$

where $r(x) = \frac{4\pi e}{\epsilon}\rho(x)$. In Glazman's paper, they assumed perfect screening of the 2DES, i.e., $U(x) = 0$ for $x > d$ (d is the depletion length). They obtained the electrostatic potential follows

$$\phi(x) = V_G\left\{\left\{\frac{1}{2} - \frac{1}{\pi}\left[\arcsin\left(\frac{2x}{d} - 1\right) + \sqrt{\frac{2x}{d}\left(2 - \frac{2x}{d}\right)}\right]\right\}\right\} \tag{4.8}$$

Considering the electrochemical equilibrium, we take the electron density in the Thomas-Fermi Approximation

$$n_s(x) = \int dE\ D(E) f(E + U(x) - \mu^*) \tag{4.9}$$

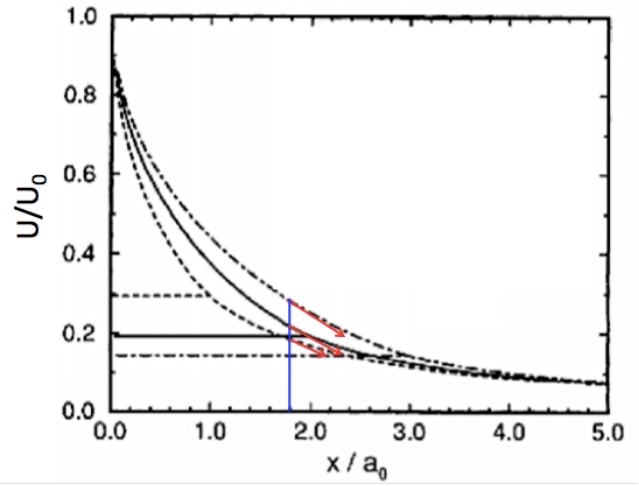

Figure 4.4 Potential or the charge density in the channel region vs distance x from the gate, for $B = 0$ T and $T = 0$ K for the depletion length $\frac{\mathrm{d}}{a_0} = 1$ (dashed line), 2 (solid line), and 3 (dash-dotted line). The horizontal lines indicate the corresponding Fermi level in units of the potential energy U_0. The red arrows represent the electric field at the blue line ($\frac{\mathrm{x}}{a_0} = 1.8$), which indicates the electric field is proportional to the gate voltage V_G. The figure we use here is adopted from Ref. 21.

with $D(E)$ the density of states (DOS), $f(E) = 1/[\exp\left(\frac{E}{k_B T}\right) + 1]$ the Fermi function, μ^* the electrochemical potential, k_B the Boltzmann constant and T the temperature. In the absence of a magnetic field, for $T = 0$, if $\phi(x) < E_F$, the total surface charge density is $\rho(x) = D_0 U(x)$ with $D_0 = \frac{m^*}{\pi\hbar^2}$. Then we obtain $a_0 r(x) = \min\{E_F, U(x)\}$ where $a_0 = \epsilon/4\pi e^2 D_0$ is the usual 2D Thomas-Fermi screening length. The depletion length is defined by the following equation: $U(d) = E_F$. With the fixed depletion length, the Eq. 4.7 reduced to a linear integral equation for $r(x)$. Figure 4.4 gives a typical numerical solution [21]. The horizontal straight lines indicate the value of E_F/U_0. As shown in the figure, U(x) has a finite slope for $x > 0$ and the depletion length increases with V_G. As indicated in the Fig. 4.4, the first derivative of $U(x)/U_0$ at $\frac{\mathrm{x}}{a_0} = 1.8$ increase a little bit as d increase, which implies ε increase as V_G increase. If we take the depletion length $d = 2a_0$, i.e. $E_F \approx 0.2U_0$, assuming $E_F = 10$ meV, the electric field at point $x = 1.8a_0$ is about 1.5×10^6 V/m.

4.3 Data analysis and results

Fig. 4.5 shows the measured magnetoresistance (MR) presented as $\Delta R = R(B) - R(B = 0)$ normalized to $R_0 = R(B = 0)$ at symmetric and asymmetric side-gate voltage as a function of B for the wide channel sample. The longitudinal resistance $R(B)$ is symmetrized by subtracting the component asymmetric in B due to the Hall-effect. Since the data is taken in a small range of B, the parabolic background can be ignored. From the measurement, a WAL peak can be found at all side-gate voltages, and the height of the peak decreases as V_G increases. We also note that universal conductance fluctuations are prominent, which may affect the fitting procedures outlined below. Future experiments are aimed at averaging out the universal conductance fluctuations at the level of the experiment itself to alleviate their potential effects.

The fitted curves in the Fig. 4.5 are fitted using the model developed by Iordanskii, Lyanda-Geller, and Pikus [24, 25], below called the ILP model. The theory incorporates k -dependent spin-precession vectors $\Omega_1(k_\parallel) = |\Omega_1|(sin\theta, -cos\theta)$ and $\Omega_3(k_\parallel) = |\Omega_3|(sin3\theta, -cos3\theta)$. In our fits, we only consider the Rashba term Ω_1 for the spin splitting ($\Omega_3 = 0$ in Refs. 24) since the Dresselhause term is negligible in our system as it arises from crystal inversion asymmetry. The correction of the conductivity can be expressed as

$$\Delta\sigma(B) = -\frac{e^2}{4\pi^2\hbar}\left(3C + \frac{1}{a_0} + \frac{2a_0+1+b_s}{a_1(a_0+b_s)-2b_s} - \sum_{n=1}^{\infty}\frac{3}{n} - \frac{3a_n^2+2b_s a_n-1-2(2n+1)b'_s}{(a_n+b_s)a_{n-1}a_{n+1}-2b_s[(2n+1)a_n-1} + 2\ln(b_{tr}) + \psi\left(\frac{1}{2}+b_\varphi\right)\right]. \quad (4.10)$$

where Ψ is the digamma function; C is Euler's constant; $a_n = b_\varphi + b_s + n + 1/2$; $b_{tr} = \hbar/4eD\tau_p B$; $b_s = 2\hbar|\Omega_1|^2\tau_p/4eDB$; $b_\varphi = \hbar/4eD\tau_\varphi B$. The diffusion coefficient D can be deduced using the two-dimensional relation $D = v_F^2\tau_p/2$, where v_F is the Fermi velocity and the transport scattering time τ_p is given by $\tau_p = \mu m^*/e$ (the electron effective mass $m^* = 0.035m_e$ at the Γ-point). The fitting parameters are provided by the characteristic magnetic fields $H_\varphi = \hbar/4eD\tau_\varphi$ and $H_{SO} = 2\hbar|\Omega_1|^2\tau_p/4eD$ respectively. Since $\Delta R(B) \ll R_0$ $\Delta\sigma(B)/\sigma(B = 0)$is approximately equal to $-\Delta R/R_0$, which allows direct comparison to experimental $R(B)$ values. We extract the values of τ_φ and Ω_1 at

different side-gate voltages according to the fittings of the experimental data, whereas N_s, D, v_F, and τ_p can be obtained from the transport (Hall and SdH) measurement.

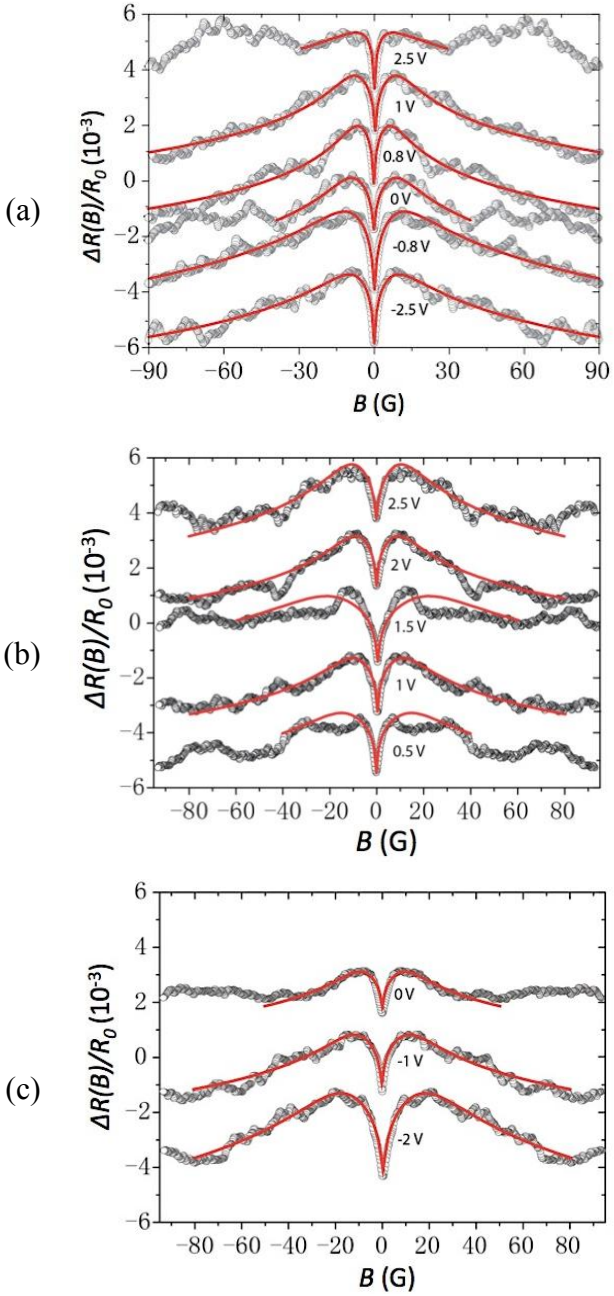

Figure 4.5 Change in magnetoresistance at a temperature of 0.4 K as a function of the applied magnetic field in the wide channel device at symmetric and asymmetric V_G: (a) symmetric V_G, (b) One gate fixed at +1.5 V, the other gate with the positive offset indicated, (c) One gate fixed at -1.5 V, the other gate with the negative offset indicated. Solid lines are fits of the magnetoconductance traces to the ILP WAL theory.

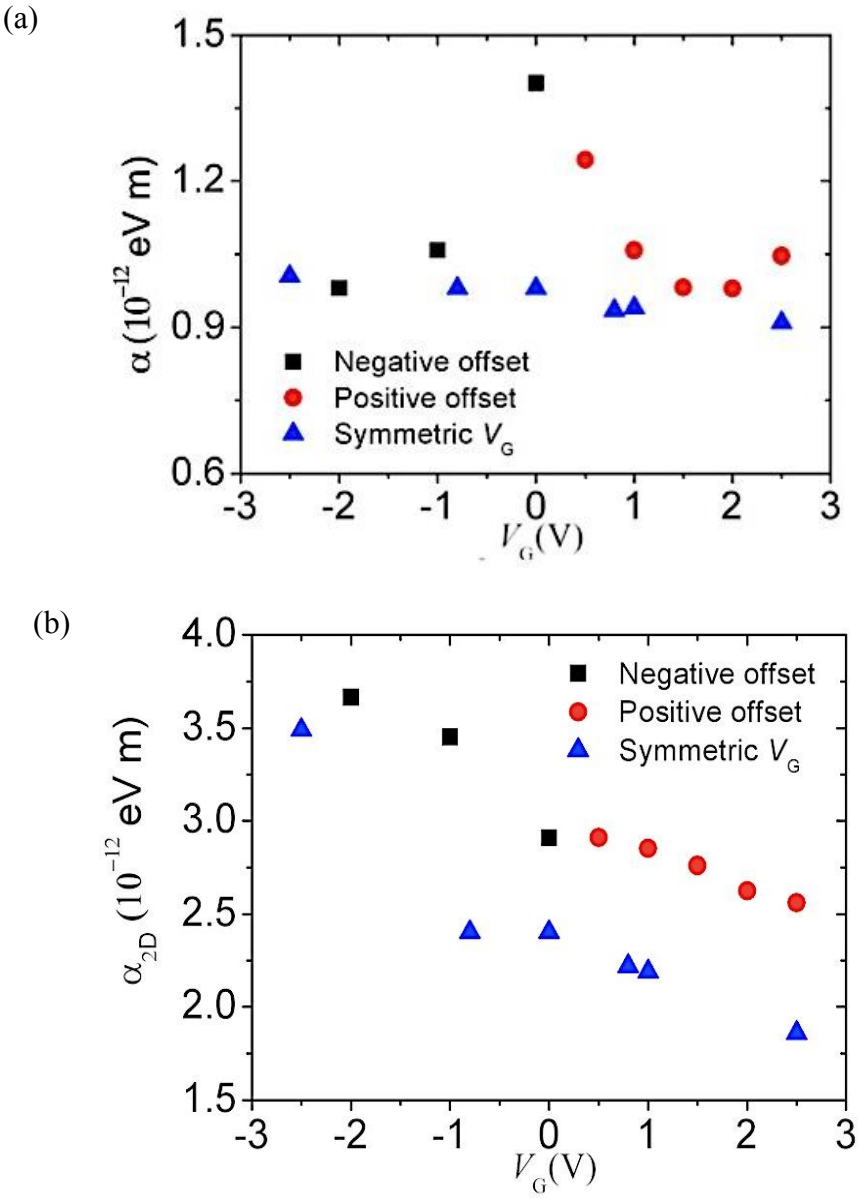

Figure 4.6 (a) The α value deduced from the WAL analysis for symmetric V_G (blue triangles) and asymmetric V_G for one gate fixed at +1.5 V, the other gate with positive offset (red dots) and one gate fixed at -1.5 V, the other gate with negative offset (black squares). (b) α_{2D} corrected for the channel width.

Although the theory is applicable in a diffusive regime ($b_{tr} > 1$), previous experiments demonstrate that it also accurately describes SOI in high mobility 2DES [25, 26]. It is noted that $\Omega_1$is defined as a half of Δ_0 ($\Delta_0 = 2\Omega_1$) in Ref. 24. Rashba SOI parameter α

values are plotted in Fig. 4.6a as a function of V_G by using the relation $\Delta_0 = 2\alpha k_F$ (with $k_F = \sqrt{2\pi N_s}$ denoting the Fermi wave vector), together with the corrected values of α_{2D}, corrected for the width w, in Fig. 4.6b. The correction arises as follows. The spin coherence length is experimentally found to depend on the ratio of the diffusion constant to the width of the channel. In a wire, $L_S = \sqrt{D\tau_S} = \sqrt{12}\frac{L_\Omega^2}{w}$, where the spin procession length $L_\Omega = \hbar^2/(2m^*\alpha)$. However in 2D, $L_S^{2D} = \sqrt{D\tau_S^{2D}} = L_\Omega$ [26]. Since $\frac{\tau_S^{2D}}{\tau_S} = \frac{\alpha^2}{\alpha_{2D}^2}$, we find the actual $\alpha_{2D} = \alpha\sqrt{12}(\frac{L_\Omega}{w})$, which is larger by a factor $\sqrt{12}(\frac{L_\Omega}{w})$ of the value α measured in the magnetoresistance. We find that, in Fig. 4.6a and b, the values of α or α_{2D} monotonically increase with increasingly negative V_G and remain almost constant for positive V_G. This implies the electric field is shielded due to the screening at $V_G > 0$. The parameter α is expected to be linearly dependent on the electric field at the 2DES ($\alpha_{2D} = \beta e\varepsilon$). For the symmetric case, if we take $\beta = 1.6 \times 10^{-18}$ m^2, the electric field $\varepsilon = 1.5 \times 10^6$ V/m at $V_G = 0$ where we have $\alpha_{2D} = 2.4 \times 10^{-12}$ eVm. At $V_G = -2.5$ V, we find $\varepsilon = 2.2 \times 10^6$ V/m, which has the order consistent with the theoretical value.

Fig. 4.7 depicts the spin coherence time τ_{SO} for symmetric and asymmetric side-gate voltage V_G. Here τ_{SO} is calculated from L_S via the diffusion constant *D*. On the asymmetric plot with positive offset with one gate fixed at +1.5 V, the value of τ_{SO} with the other gate at +1.5 V, is 1.4 ps. However, on the symmetric plot, $\tau_{SO} = 1.535$ ps with both gates fixed at +1.5 V. This behavior of τ_{SO} indicates that the results are subject to electric field hysteresis as function of the gate voltages. On the asymmetric plot with negative offset with one gate fixed at -1.5 V, the value of τ_{SO} with the other gate at -1.5 V is 0.9 ps. Thus negative V_G gives a lower τ_{SO}, meaning a stronger SOI, which is also consistent with above.

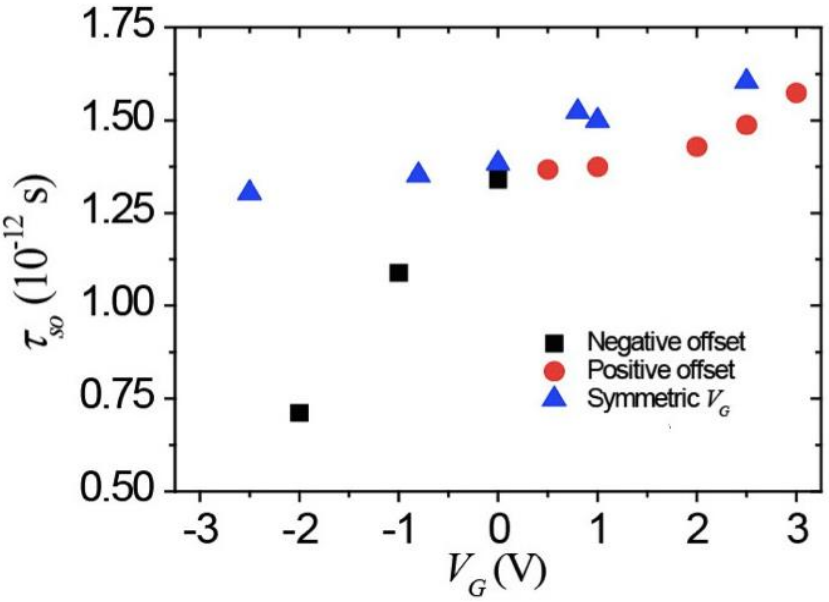

Figure 4.7 The spin coherence time τ_{SO} for symmetric and asymmetric application of side-gate voltages V_G. Data is shown by blue triangles for symmetric V_G. For asymmetric V_G either one gate voltage was held at at +1.5 V, and the other gate voltage varied with a positive offset from +1.5 V (red dots) or one gate voltage was held at -1.5 V, and the other gate voltage varied with a negative offset from -1.5 V (black squares).

For the narrower channel, we obtained similar results when applying symmetric side-gate voltages, as shown in Fig. 4.8. The corrected α_{2D} is much larger than that of the wide channel, which may imply that the width correction is overemphasized.

In summary, we fabricated side-gated structures to study the tunability of the SOI in mesoscopic InGaAs channels. Our data provides evidence that the side-gate voltages can tune the SOI without appreciably changing the electron density in the channel. The order of magnitude of the electric fields deduced from the SOI is compatible with our calculations. While our data shows tunability, especially for negative side-gate voltages, the data and the simulations considered together leave open the possibility that the component of the electric field normal to the 2DES lies at the origin of the tunability.

(a)

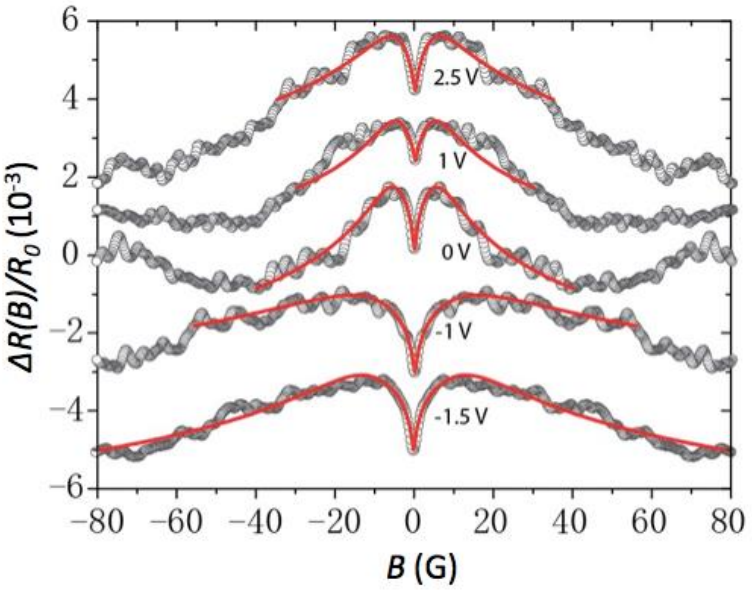

(b)

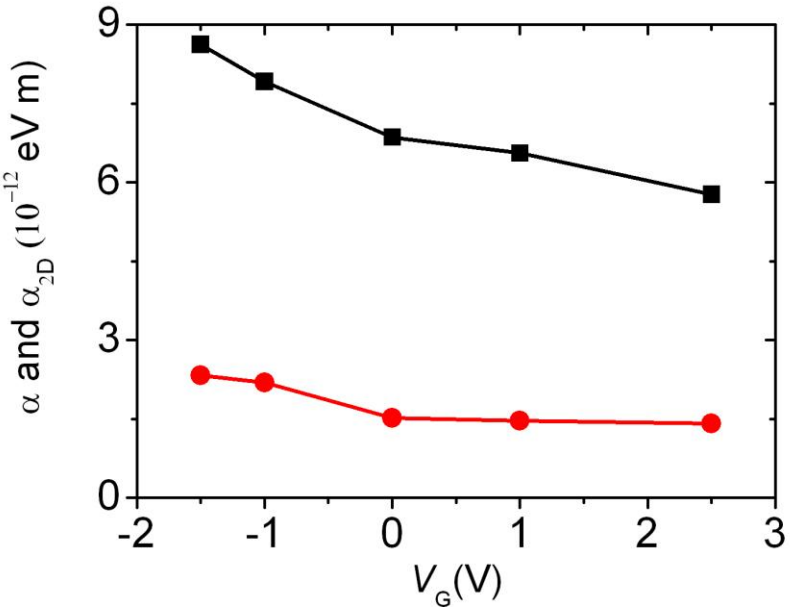

Figure 4.8 (a) Change in magnetoresistance at a temperature of 0.4 K, $\Delta\sigma$, as a function of the applied magnetic field in the narrow channel device for symmetric application of side-gate voltages V_G, for different values of V_G. (b) The corresponding α and α_{2D} at the different applied side-gate voltages.

4.4 References

1. L. Xu, S. Ren and J. J. Heremans *Integr. Ferroelectr.* **131** 36–46 (2011).

2. S. Datta and B. Das, Appl. Phys. Lett. 56, 665 (1990).

3. A. G. Aronov and Y. B. Lyanda-Geller, Phys. Rev. Lett. 70, 343 (1993).

4. T. Koga et al., Phys. Rev. Lett. 88, 126601 (2002).

5. A. Kiselev and K. Kim, Appl. Phys. Lett. 78, 775 (2001).

6. J. Nitta, T. Akazaki, H. Takayanagi and T. Enoki, Phys. Rev. Lett. 78, 1335 (1997).

7. G. Lommer, F. Malcher, and U. Rössler, Phys. Rev. Lett. 60, 728 (1988).

8. J. Luo, H. Munekata, F. F. Fang, and P. J. Stiles, Phys. Rev. B 38, 10, 142 (1988).

9. E. de Andrada e Silva, G. C. L. Rocca, and F. Bassani, Phys. Rev. B 50, 8523 (1994).

10. E. de Andrada e Silva, G. C. L. Rocca, and F. Bassani, Phys. Rev. B 55, 16293 (1997).

11. J. B. Miller, D. M. Zumb¨uhl, C. M. Marcus, Y. B. LyandaGeller, D. Goldhaber-Gordon, K. Campman, and A. C. Gossard, 2003, Phys. Rev. Lett. 90, 076807, (2003).

12. P. Debray, S.M.S. Rahman, J. Wan, R.S. Newrock, M. Cahay, A.T. Ngo, S.E. Ulloa, S.T. Herbert, M. Muhammad and M. Johnson, Nature Nanotechnol. 4, 759 (2009).

13. M. Kohda, S. Nakamura, Y. Nishihara, K. Kobayashi, T. Ono, J. Ohe, Y. Tokura, T. Mineno, J. Nitta, Nature Communications 3, 1038 (2012).

14. B. Das, D.C. Miller, S. Datta, R. Reifenberger, W.P. Hong, P.K. Bhattacharaya, J. Singh, and M. Jaffe, Phys. Rev. B 39, 1411 (1989).

15. D. R. Leadley, R. Fletcher, R. J. Nicholas, F. Tao, C. T. Foxon, and J. J. Harris, Phys. Rev. B 46, 12439 (1992).

16. 9 S. Brosig, K. Ensslin, R. J. Warburton, C. Nguyen, B. Brar, M. Thomas, and H. Kroemer, Phys. Rev. B 60, R13989 (1999).

17. N. Thillosen, S. Caba˜nas, N. Kaluza, V. A. Guzenko, H. Hardtdegen, and Th. Sch¨apers, Phys. Rev. B 73, 241311(R) (2006).

18. Guzenko, V. A.; Sch¨apers, T.; Hardtdegen, H. Phys. Rev. B, 76, 165301 (2007).

19. A E Kavruk, T Ozturk, A Ozturk, U Atav and H Yuksel, J. Physics: Conference Series 334 (2011).

20. A. Siddiki and F. Marquardt, Phys. Rev. B 75, 045325 (2007).

21. K. Lier and R. R. Gerhardts, Phys. Rev. B 50, 7757 (1994).

22. D. B. Chklovskii, B. I. Shklovskii, L. I. Glazman, Phys. Rev. B 46, 4026 (1992).

23. J. Davies, I. A. Larkin, and E. V. Sukhorukov, J. Appl. Phys. 77, 4504 (1995).

24. S. V. Iordanskii, Y. B. Lyanda-Geller, and G. E. Pikus, JETP Lett. 60, 206 (1994).

25. T. Koga, J. Nitta, T. Akazaki and H. Takayanagi, Phys. Rev. Lett. 89, 04681 (2002).

26. R. L. Kallaher, J. J. Heremans, N. Goel, S. J. Chung, and M. B. Santos, Phys. Rev. B 81, 075303 (2010).

Chapter 5. Summary

Spintronics is considered to be an excellent avenue for future electronics. To realize semiconductor-base spintronics devices, the key is the manipulation of the electron spin. The Aharonov-Casher (AC) effect may present avenues for electrical control of spin and magnetic moments in magnetoelectronics. In this thesis, we studied the AC effect in a narrow channel. Similarly to the integer quantum Hall effect, edge states are predicted to exist, with properties similar to the edge states in the quantum spin Hall effect. The propagation direction of the AC edge states depends on the orientation of the magnetic moment. Along a given edge, for magnetic moments of opposite orientations, the edge states move in opposite directions. It was found that the interference phenomena can be caused by the AC flux, as is the case for the Aharonov-Bohm (AB) flux. One can construct an argument whereby a temporal change in AB flux by h/e will create a current to transport a unit charge e, leading to a quantum of conductance e^2/h. In AC effect, the quantization of the charge conductivity is replaced by quantized magnetization transport. Since the magnetic moment is not a fundamental constant compared to charge, it is difficult to detect the corresponding magnetization transport directly. Yet, the AC effect may create avenues of using electric fields to control the spin and magnetic moments in magnetoelectronics, which is important for spintronics.

We fabricated antidots in narrow short mesoscopic channels to access the AC phase and the AC edge states in two-dimensional electron systems confined to quantum wells in a InGaAs/InAlAs heterostructure. The low-temperature (0.4 K and 1.2 K) quantum transport measurements were conducted in ^{3}He or in ^{4}He cryostats with lock-in techniques under applied tilted magnetic fields, and mostly consist of magnetoresistance measurements. With magnetic fields nearly in-plane of the quantum well, we observe fine structure with mT spacing, which we tentatively ascribe to the AC edge state energy spacing. Due to the strong Rashba spin-orbit interaction in the material itself, the effects of spin rotation are small and its effects on quantum transport are expected to be moderate and smooth in applied magnetic field. Thus, the fine structure in the magnetoresistance measurements is instead ascribed to the energy spacing between AC

edge states, forming tentative experimental evidence for AC edge states in mesoscopic channels.

The data obtained on the channels with antidots have a complex magnetoresistance structure, and more information was needed on the strength of the effective vector potential associated with the AC effect. To that effect, we fabricated side-gated channels with different width on the same heterostructure material, to study the tunabilty of the spin-orbit interaction. The values of the strength of spin-obit interaction constant α at different side-gate voltages were obtained by analyzing the weak antilocalization according to a specific model suitable for Rashba spin-orbit interaction in low-dimensional systems. Our results show that the strength of the spin-orbit interaction can be manipulated by the side-gate voltages without appreciably changing the electron density in the channel. The data and the simulations in this thesis leave open the possibility that the normal component of the electric field leads to the tenability of the spin-orbit interaction, as we cannot ascertain which component of the electric field is responsible. Simulations of the electric fields in the mesoscopic channel structures indeed indicate the three-dimensional nature of the electric fields, and indicate that the order of magnitude of the electric fields deduced from the experimental values of the spin-orbit interaction are compatible with our calculations. The experimental results for the spin-obit interaction constant α were corrected for width, showing that the corrected values have a strong correlation with the side-gate voltages, especially for the negative side-gate voltages. We compare spin-obit interaction constant α values between symmetrically and asymmetrically applied side-gate voltages. The results reinforce the conclusions that negative side-gate voltage yield higher spin-obit interaction constants. Experimentally, narrower channels yield similar but higher spin-obit interaction constants, which may either indicate that the correction for width is somewhat overemphasized, or that electric fields are indeed stronger in narrower channels.